

Hierarchical Neyman-Pearson Classification for Prioritizing Severe Disease Categories in COVID-19 Patient Data

Lijia Wang *

Department of Mathematics, University of Southern California

Y. X. Rachel Wang * †

School of Mathematics and Statistics, University of Sydney

Jingyi Jessica Li

Department of Statistics, University of California, Los Angeles

Xin Tong

Department of Data Sciences and Operations, University of Southern California

October 6, 2022

Abstract

COVID-19 has a spectrum of disease severity, ranging from asymptomatic to requiring hospitalization. Providing appropriate medical care to severe patients is crucial to reduce mortality risks. Hence, in classifying patients into severity categories, the more important classification errors are “under-diagnosis”, in which patients are misclassified into less severe categories and thus receive insufficient medical care. The Neyman-Pearson (NP) classification paradigm has been developed to prioritize the designated type of error. However, current NP procedures are either for binary classification or do not provide high probability controls on the prioritized errors in multi-class classification. Here, we propose a hierarchical NP (H-NP) framework and an umbrella algorithm that generally adapts to popular classification methods and controls the under-diagnosis errors with high probability. On an integrated collection of single-cell RNA-seq (scRNA-seq) datasets for 740 patients, we explore ways of featurization and demonstrate the efficacy of the H-NP algorithm in controlling the under-diagnosis errors regardless of featurization. Beyond COVID-19 severity classification, the H-NP algorithm generally applies to multi-class classification problems, where classes have a priority order.

*Equal contribution

†Correspondence should be addressed to Y.X. Rachel Wang (rachel.wang@sydney.edu.au)

1 Introduction

The COVID-19 pandemic has infected more than 615 million people and caused 6.54 million deaths (September 24th, 2022), prompting collective efforts from statistics and other communities to address data-driven challenges. Many statistical works have modeled the COVID-19 epidemic dynamics [Betensky and Feng, 2020, Quick et al., 2021], forecasted the case growth rates and outbreak locations [Brooks et al., 2020, Tang et al., 2021, McDonald et al., 2021], and analyzed and predicted the mortality rates [James et al., 2021, Kramlinger et al., 2022]. Classification problems, such as COVID-19 diagnosis (positive/negative) [Wu et al., 2020, Li et al., 2020, Zhang et al., 2021] and severity prediction [Yan et al., 2020, Sun et al., 2020, Zhao et al., 2020, Ortiz et al., 2022], have been tackled by machine learning approaches (e.g., logistic regression, support vector machine (SVM), random forest, boosting, and neural network; see Alballa and Al-Turaiki [2021] for a review). In the existing COVID-19 classification works, the commonly used data types are CT images, routine blood tests, and other clinical data including age, blood pressure and medical history. In comparison, multiomics data are harder to acquire but can provide better insights into the molecular features driving patient responses to the disease [Overmyer et al., 2021]. Recently, the increasing availability of single-cell RNA-seq (scRNA-seq) data offers the opportunity to understand transcriptional responses to COVID-19 severity at the cellular level [Wilk et al., 2020, Stephenson et al., 2021, Ren et al., 2021]. In this study, we focus on patient severity classification using an integrated collection of multi-patient blood scRNA-seq datasets.

Based on the WHO guidelines [World Health Organization, 2020], COVID-19 patients have at least three severity categories: healthy, mild/moderate, and severe. Severity classification is essential for providing appropriate medical care and reducing fatality rates. The classical classification paradigm aims at minimizing the overall classification error. How-

ever, in severity classification, the “under-diagnosis” errors (i.e., misclassifying a patient into a less severe category) should be prioritized in the classification objective because they can result in insufficient medical treatments and elevated mortality risks.

Motivated by the gap in existing classification algorithms for severity classification (Section 1.1), we propose a hierarchical Neyman-Pearson (H-NP) classification framework that prioritizes the under-diagnosis error control in the following sense. Suppose there are \mathcal{I} classes with class labels $[\mathcal{I}] = \{1, 2, \dots, \mathcal{I}\}$ ordered in decreasing severity. For $i \in [\mathcal{I} - 1]$, the i -th under-diagnosis error is the probability of misclassifying an individual in class i into any class j with $j > i$. We develop an H-NP umbrella algorithm that controls the i -th under-diagnosis error below a user-specified level $\alpha_i \in (0, 1)$ with high probability while minimizing a weighted sum of the remaining classification errors. Similar in spirit to the NP umbrella algorithm for binary classification in [Tong et al. \[2018\]](#), the H-NP umbrella algorithm adapts to popular scoring-type multi-class classification methods (e.g., logistic regression, random forest, and SVM). To our knowledge, the algorithm is the first to achieve asymmetric error control with high probability in multi-class classification.

Another contribution of this study is the exploration of appropriate ways to featurize multi-patient scRNA-seq data. Following the workflow in [Lin et al. \[2020a\]](#), we integrate nine publicly available scRNA-seq datasets to form a sample of 740 patients with three levels of severity. For each patient, scRNA-seq data were collected from peripheral blood mononuclear cells (PBMCs) and processed into a sparse expression matrix, which consists of tens of thousands of genes in rows and thousands of cells in columns. We propose four ways of extracting a feature vector from each of these 740 matrices. Then we evaluate the performance of each featurization way in combination with multiple classification methods under both the classical and H-NP classification paradigms. We note that our H-NP

umbrella algorithm is applicable to other featurizations of scRNA-seq data, other forms of patient data, and more general disease classification problems with a severity ordering.

Below we review the NP paradigm and featurization of multi-patient scRNA-seq data as the background of our work.

1.1 Neyman-Pearson paradigm and multi-class classification

Classical binary classification focuses on minimizing the overall classification error, i.e., a weighted sum of type I and II errors, where the weights are the marginal probabilities of the two classes. However, the class priorities are not reflected by the class weights in many applications, especially severe disease diagnosis, where the severe class is the minor class and has a smaller weight (e.g., HIV [Meyer and Pauker, 1987] and cancer [Dettling and Bühlmann, 2003]). The NP classification paradigm [Cannon et al., 2002, Scott and Nowak, 2005, Rigollet and Tong, 2011] was developed to enforce class priorities: it finds a classifier that controls the population type I error (the prioritized error, e.g., misclassifying diseased patients as healthy) under a user-specified level α while minimizing the type II error (the error with less priority, e.g., misdiagnosing healthy people as sick). Practically, using an order statistics approach, Tong et al. [2018] proposed an NP umbrella algorithm that adapts all scoring-type classification methods (e.g., logistic regression) to the NP paradigm for classifier construction. The resulting classifier has the population type I error under α with high probability. Besides disease diagnosis, the NP classification paradigm has found diverse applications, including social media text classification [Xia et al., 2021] and crisis risk control [Feng et al., 2021]. Nevertheless, the original NP paradigm is for binary classification only.

Although several works aimed to control prioritized errors in multi-class classification [Landgrebe and Duin, 2005, Xiong et al., 2006, Tian and Feng, 2021], they did not provide

high probability control. That is, if they are applied to severe disease classification, there is a non-trivial chance that their under-diagnosis errors exceed the desired levels.

1.2 ScRNA-seq data featurization

In multi-patient scRNA-seq data, every patient has a gene-by-cell expression matrix, which contains the expression levels of genes in cells; genes are matched across patients, but cells are not. For learning tasks with patients as instances, featurization is a necessary step to ensure that all patients have features in the same space. A common featurization approach is to assign every patient’s cells into cell types, which are comparable across patients, by clustering [Stanley et al., 2020, Ganio et al., 2020] and/or manual annotation [Han et al., 2019]. Then, each patient’s gene-by-cell expression matrix can be converted into a gene-by-cell-type expression matrix using a summary statistic (e.g., every gene’s mean expression in a cell type), so all patients have gene-by-cell-type expression matrices with the same dimensions. We note here that most of the previous multi-patient single-cell studies with a reasonably large cohort used CyTOF data [Davis et al., 2017], which typically measures 50–100 protein markers, whereas scRNA-seq data has a much higher feature dimension, containing expression values of $\sim 10^4$ genes. Thus further featurization is necessary to convert each patient’s gene-by-cell-type expression matrix into a feature vector for classification.

Following the data processing workflow in Lin et al. [2020a], we obtain 740 patients’ cell-type-by-gene expression matrices, which include 19 cell types and 3000 genes (after filtering). We propose and compare four ways of featurizing these matrices into vectors. The four ways differ in their treatments of 0 values and approaches for dimension reduction. Note that we perform featurization as a separate step before classification so that all classification methods are applicable. Separating the featurization step also allows us to

investigate whether a featurization way maintains robust performance across classification methods.

The rest of the paper is organized as follows. In Section 2, we introduce the H-NP classification framework and propose an umbrella algorithm to control the under-diagnosis errors with high probability. Next, we conduct simulation studies to evaluate the performance of the umbrella algorithm. In Section 3, we describe the four ways of featurizing the COVID-19 multi-patient scRNA-seq data and show their performance with multiple classification methods under the H-NP classification framework. We also show that the H-NP umbrella algorithm consistently controls the under-diagnosis errors in COVID-19 severity classification across featurization ways and classification methods. Supplementary Materials contain the technical derivations and proofs.

2 Hierarchical Neyman-Pearson (H-NP) classification

2.1 Under-diagnosis errors in H-NP classification

We first introduce the formulation of H-NP classification and define the under-diagnosis errors, which are the probabilities of individuals being misclassified to less severe (more generally, less important) classes. In an H-NP problem with $\mathcal{I} \geq 2$ classes, the class labels $i \in [\mathcal{I}] := \{1, 2, \dots, \mathcal{I}\}$ are ranked in a decreasing order of importance, i.e., class i is more important than class j if $i < j$. Let (X, Y) be a random pair, where $X \in \mathcal{X} \subset \mathbb{R}^d$ represents a vector of features, and $Y \in [\mathcal{I}]$ denotes the class label. A classifier $\phi : \mathcal{X} \rightarrow [\mathcal{I}]$ maps a feature vector X to a predicted class label. In the following discussion, we abbreviate $\mathbb{P}(\cdot \mid Y = i)$ as $P_i(\cdot)$. Our H-NP framework aims to control the under-diagnosis errors at the population level in the sense that

$$R_{i\star}(\phi) = P_i(\phi(X) \in \{i + 1, \dots, \mathcal{I}\}) \leq \alpha_i \quad \text{for } i \in [\mathcal{I} - 1], \quad (1)$$

where $\alpha_i \in (0, 1)$ is the desired control level for the i -th under-diagnosis error $R_{i\star}(\phi)$. Simultaneously, our H-NP framework minimizes the weighted sum of the remaining errors, which can be expressed as

$$R^c(\phi) = \mathbb{P}(\phi(X) \neq Y) - \sum_{i=1}^{\mathcal{I}-1} \pi_i R_{i\star}(\phi), \quad \text{where } \pi_i = \mathbb{P}(Y = i). \quad (2)$$

We note that when $\mathcal{I} = 2$, this H-NP formulation is equivalent to the binary NP classification paradigm (prioritizing class 1 over class 2), with $R_{1\star}(\phi)$ being the population type I error.

For COVID-19 severity classification with three levels, severe patients labeled as $Y = 1$ have the top priority, and we want to control the probability of severe patients not being identified, which is $R_{1\star}(\phi)$. The secondary priority is for moderate patients labeled as $Y = 2$; $R_{2\star}(\phi)$ is the probability of moderate patients being classified as healthy. Healthy patients that do not need medical care are labeled as $Y = 3$. Note that $R_{i\star}(\cdot)$ and $R^c(\cdot)$ are population-level quantities as they depend on the intrinsic distribution of (X, Y) , and it is hard to control the $R_{i\star}(\cdot)$'s almost surely due to the randomness of the classifier.

2.2 H-NP algorithm with high probability control

In this section, we construct an H-NP umbrella algorithm that controls the population under-diagnosis errors in the sense that $\mathbb{P}(R_{i\star}(\hat{\phi}) > \alpha_i) \leq \delta_i$ for $i \in [\mathcal{I} - 1]$, where $(\delta_1, \dots, \delta_{\mathcal{I}-1})$ is a vector of tolerance parameters, and $\hat{\phi}$ is a scoring-type classifier to be defined below.

Roughly speaking, we employ a sample-splitting strategy, which uses some data subsets to train the scoring functions from a base classification method (e.g., output from the softmax transformation in multinomial logistic regression) and other data subsets to select

appropriate thresholds on the scores to achieve population-level error controls. For $i \in [\mathcal{I}]$, let $\mathcal{S}_i = \{X_j^i\}_{j=1}^{n_i}$ denote n_i independent observations from class i , where n_i is the size of the class. In the following discussion, the superscript on X is dropped for brevity when it is clear which class the observation comes from. Our procedure randomly splits the class- i observations into (up to) three parts: \mathcal{S}_{is} ($i \in [\mathcal{I}]$) for obtaining scoring functions, \mathcal{S}_{it} ($i \in [\mathcal{I} - 1]$) for selecting thresholds, and \mathcal{S}_{ie} ($i = 2, \dots, \mathcal{I}$) for computing empirical errors. As will be made clear later, \mathcal{S}_{1e} and $\mathcal{S}_{\mathcal{I}t}$ are not needed in our procedure, and we only split class 1 and class \mathcal{I} into two parts. After splitting, we use the combination of observations $\mathcal{S}_s = \bigcup_{i \in [\mathcal{I}]} \mathcal{S}_{is}$ to train the scoring functions.

We consider a classifier that relies on $\mathcal{I} - 1$ scoring functions $T_1, T_2, \dots, T_{\mathcal{I}-1} : \mathcal{X} \rightarrow \mathbb{R}$, where the class decision is made sequentially with each $T_i(X)$ determining whether the observation belongs to class i or one of the less prioritized classes $(i + 1), \dots, \mathcal{I}$. Thus at each step i , the decision is binary, allowing us to use the NP Lemma to motivate the construction of our scoring functions. Note that $\mathbb{P}(Y = i \mid X = x) / \mathbb{P}(Y \in \{i + 1, \dots, \mathcal{I}\} \mid X = x) \propto f_i(x) / f_{>i}(x)$, where $f_{>i}(x)$ and $f_i(x)$ represent the density function of X when $Y > i$ and $Y = i$, respectively, and the density ratio is the statistic that leads to the most powerful test with a given level of control on one of the errors by the NP Lemma. Given a typical scoring-type classification method (e.g., logistic regression, random forest, SVM, and neural network) that provides the probability estimates $\widehat{\mathbb{P}}(Y = i \mid X)$ for $i \in [\mathcal{I}]$, we can construct our scores using these estimates by defining

$$T_1(X) = \widehat{\mathbb{P}}(Y = 1 \mid X), \quad \text{and} \quad T_i(X) = \frac{\widehat{\mathbb{P}}(Y = i \mid X)}{\sum_{j=i+1}^{\mathcal{I}} \widehat{\mathbb{P}}(Y = j \mid X)} \quad \text{for } 1 < i < \mathcal{I} - 1.$$

Given thresholds $(t_1, t_2, \dots, t_{\mathcal{I}-1})$, we consider an H-NP classifier of the form

$$\widehat{\phi}(X) = \begin{cases} 1, & T_1(X) \geq t_1; \\ 2, & T_2(X) \geq t_2 \quad \text{and} \quad T_1(X) < t_1; \\ \dots & \\ \mathcal{I} - 1, & T_{\mathcal{I}-1}(X) \geq t_{\mathcal{I}-1} \quad \text{and} \quad T_1(X) < t_1, \dots, T_{\mathcal{I}-2}(X) < t_{\mathcal{I}-2}; \\ \mathcal{I}, & \text{otherwise.} \end{cases} \quad (3)$$

Then the i -th under-diagnosis error for this classifier can be written as

$$R_{i\star}(\widehat{\phi}) = P_i(\widehat{\phi}(X) \in \{i+1, \dots, \mathcal{I}\}) = P_i(T_1(X) < t_1, \dots, T_i(X) < t_i), \quad (4)$$

where X is a new observation from the i -th class independent of the data used for score training and threshold selection. The thresholds $(t_1, t_2, \dots, t_{\mathcal{I}-1})$ are selected using the observations in $\mathcal{S}_{1t}, \dots, \mathcal{S}_{(\mathcal{I}-1)t}$, and they are chosen to satisfy $\mathbb{P}(R_{i\star}(\widehat{\phi}) > \alpha_i) \leq \delta_i$ for all $i \in [\mathcal{I} - 1]$. In what follows, we will develop our arguments conditional on the data \mathcal{S}_s for training the scoring functions so that T_i 's can be viewed as fixed functions.

According to Eq (3), the first under-diagnosis error $R_{1\star}(\widehat{\phi}) = P_1(T_1(X) < t_1)$ only depends on t_1 , while the other under-diagnosis errors $R_{i\star}(\widehat{\phi})$ depend on t_1, \dots, t_i . To achieve the high probability controls with $\mathbb{P}(R_{i\star}(\widehat{\phi}) > \alpha_i) \leq \delta_i$ for all $i \in [\mathcal{I} - 1]$, we select $t_1, \dots, t_{\mathcal{I}-1}$ sequentially using an order statistics approach. We start with the selection of t_1 , which is covered by the following general proposition. The proof is a modification of Proposition 1 in [Tong et al. \[2018\]](#) and can be found in Supplementary Materials [B.1](#).

Proposition 1. *For any $i \in [\mathcal{I}]$, denote $\mathcal{T}_i = \{T_i(X) \mid X \in \mathcal{S}_{it}\}$, and let $t_{i(k)}$ be the*

corresponding k -th order statistic. Further denote the cardinality of \mathcal{T}_i as n_i . Assuming that the data used to train the scoring functions and the left-out data are independent, then given a control level α , for another independent observation X from class i ,

$$\mathbb{P} \left(P_i [T_i(X) < t_{i(k)} \mid t_{i(k)}] > \alpha \right) \leq v(k, n_i, \alpha) := \sum_{j=0}^{k-1} \binom{n_i}{j} (\alpha)^j (1 - \alpha)^{n_i - j}. \quad (5)$$

Algorithm 1: DeltaSearch(n, α, δ)

Input : size: n ; level: α ; tolerance: δ .

1 $k = 0, v_k = 0$
2 **while** $v_k \leq \delta$ **do**
3 $v_k = v_k + \binom{n}{k} (\alpha)^k (1 - \alpha)^{n-k}$
4 $k = k + 1$
5 **end**

Output: k

Let $k_i = \max\{k \mid v(k, n_i, \alpha_i) \leq \delta_i\}$, which can be computed using Algorithm 1. Then Proposition 1 and Eq (4) imply

$$\mathbb{P} \left(R_{i\star}(\hat{\phi}) > \alpha_i \right) \leq \mathbb{P} \left(P_i [T_i(X) < t_i \mid t_{i(k_i)}] > \alpha_i \right) \leq \delta_i \quad \text{for all } t_i \leq t_{i(k_i)}. \quad (6)$$

We note that to have a solution for $v(k, n_i, \alpha_i) \leq \delta_i$ among $k \in [n_i]$, we need $n_i \geq \log \delta_i / \log(1 - \alpha_i)$, the minimum sample size required for the class \mathcal{S}_{it} . When $i = 1$, the first inequality in Eq (6) in fact becomes equality, so $t_{1(k_1)}$ is an effective upper bound on t_1 when we later minimize the empirical counterpart of $R^c(\cdot)$ in Eq (2) with respect to different feasible threshold choices. On the other hand, for $i > 1$, the inequality is mostly strict, which means that the bound $t_{i(k_i)}$ on t_i is expected to be loose and can be improved. To this end, we note that Eq (4) can be decomposed as $R_{i\star}(\hat{\phi}) = P_i (T_i(X) < t_i \mid T_1(X) < t_1, \dots, T_{i-1}(X) < t_{i-1}) \cdot P_i (T_1(X) < t_1, \dots, T_{i-1}(X) < t_{i-1})$, leading to the following theorem that finds the upper bound on t_i given the previous thresholds.

Theorem 1. *Given the previous thresholds t_1, \dots, t_{i-1} , consider all the scores T_i on the left-out class \mathcal{S}_{it} , $\mathcal{T}_i = \{T_i(X) \mid X \in \mathcal{S}_{it}\}$, and a subset of these scores depending on the previous thresholds, defined as $\mathcal{T}'_i = \{T_i(X) \mid X \in \mathcal{S}_{it}, T_1(X) < t_1, \dots, T_{i-1}(X) < t_{i-1}\}$. We use $t_{i(k)}$ and $t'_{i(k)}$ to denote the k -th order statistic of \mathcal{T}_i and \mathcal{T}'_i , respectively. Let n_i and n'_i be the cardinality of \mathcal{T}_i and \mathcal{T}'_i , respectively, and α_i and δ_i be the prespecified control level and violation tolerance for the i -th under-diagnosis error $R_{i\star}(\cdot)$. We set*

$$\hat{p}_i = \frac{n'_i}{n_i}, p_i = \hat{p}_i + c(n_i), \alpha'_i = \frac{\alpha_i}{p_i}, \delta'_i = \delta_i - \exp\{-2n_i c^2(n_i)\}, \quad (7)$$

where $c(n) = \mathcal{O}(1/\sqrt{n})$. Let

$$\bar{t}_i = \begin{cases} t'_{i(k'_i)}, & \text{if } n'_i \geq \log \delta'_i / \log(1 - \alpha'_i) \quad \text{and} \quad \alpha'_i < 1; \\ t_{i(k_i)}, & \text{otherwise,} \end{cases} \quad (8)$$

where $k_i = \max\{k \in [n_i] \mid v(k, n_i, \alpha_i) \leq \delta_i\}$ and $k'_i = \max\{k \in [n'_i] \mid v(k, n'_i, \alpha'_i) \leq \delta'_i\}$.

Then,

$$\mathbb{P}(R_{i\star}(\hat{\phi}) > \alpha_i) = \mathbb{P}(P_i [T_1(X) < t_1, \dots, T_i(X) < t_i \mid \bar{t}_i] > \alpha_i) \leq \delta_i \quad \text{for all } t_i \leq \bar{t}_i. \quad (9)$$

In other words, if the cardinality of \mathcal{T}'_i exceeds a threshold, we can refine the choice of the upper bound according to Eq (8); otherwise, the bound in Proposition 1 always applies. The proof of the theorem is provided in Supplementary Materials B.2; the computation of the upper bound \bar{t}_i is summarized in Algorithm 2. \bar{t}_i guarantees the required high probability control on the i -th under-diagnosis error, while providing a tighter bound compared with Eq (4). We make two additional remarks as follows.

Remark 1. a) *The minimum sample size requirement for \mathcal{S}_{it} is still $n_i \geq \log \delta_i / \log(1 - \alpha_i)$ because $t_{i(k_i)}$ in Eq (8) always exists when this inequality holds. For instance, if $\alpha_i = 0.05$ and $\delta_i = 0.05$, then $n_i \geq 59$.*

b) *The choice of $c(n)$ involves a trade-off between α'_i and δ'_i , although under the constraint $c(n) = \mathcal{O}(1/\sqrt{n})$, any changes in both quantities are small in magnitude for large n . For example, a larger $c(n)$ leads to a smaller α'_i and a larger δ'_i , thus a looser tolerance level comes at the cost of a stricter error control level. In practice, larger α'_i and larger δ'_i values are desired since they lead to a wider region for t_i . We set $c(n) = 2/\sqrt{n}$ throughout the rest of the paper. Then by Eq (7), α'_i increases as n increases, and $\delta'_i = \delta_i - e^{-4}$, so the difference between δ'_i and the prespecified δ_i is sufficiently small.*

With the set of upper bounds on the thresholds chosen according to Theorem 1, the next step is to find an optimal set of thresholds $(t_1, t_2, \dots, t_{\mathcal{I}-1})$ satisfying these upper bounds while minimizing the empirical version of $R^c(\hat{\phi})$, which is calculated using observations in $\mathcal{S}_e = \bigcup_{i=2}^{\mathcal{I}} \mathcal{S}_{ie}$ (since class-1 observations are not needed in $R^c(\hat{\phi})$). For brevity, we denote all the empirical errors as \tilde{R} , e.g., \tilde{R}^c . In Section 2.4, we will show numerically that Theorem 1 provides a wider search region for the threshold t_i compared to Proposition 1, which benefits the minimization of R^c .

As our COVID-19 data has three severity levels, in the next section, we will focus on the three-class H-NP umbrella algorithm and describe in more details how the above procedures can be combined to select the optimal thresholds in the final classifier.

2.3 H-NP umbrella algorithm for three classes

Since our COVID-19 data groups patients into three severity categories, we introduce our H-NP umbrella algorithm for $\mathcal{I} = 3$. In this case, there are two under-diagnosis errors

Algorithm 2: UpperBound($\mathcal{S}_{it}, \alpha_i, \delta_i, (T_1, \dots, T_i), (t_1, \dots, t_{i-1})$)

Input : The left-out class- i samples: \mathcal{S}_{it} ; level: α_i ; tolerance: δ_i ; score functions: (T_1, \dots, T_i) ; thresholds: (t_1, \dots, t_{i-1}) .

```

1  $n_i \leftarrow |\mathcal{S}_{it}|$ 
2  $\{t_{i(1)}, \dots, t_{i(n_i)}\} \leftarrow \text{sort } \mathcal{T}_i = \{T_i(X) \mid X \in \mathcal{S}_{it}\}$ 
3  $k_i \leftarrow \text{DeltaSearch}(n_i, \alpha_i, \delta_i)$ 
4  $\bar{t}_i \leftarrow t_{i(k_i)}$ 
5 if  $i > 1$  then
6    $\mathcal{T}'_i \leftarrow \{t'_{i(1)}, \dots, t'_{i(n'_i)}\} = \text{sort}\{T_i(X) \mid X \in \mathcal{S}_{it}, T_1(X) < t_1, \dots, T_{i-1}(X) < t_{i-1}\}$ ;
   // Note that  $n'_i$  is random
7    $\hat{p}_i \leftarrow \frac{n'_i}{n_i}$ ,  $p_i \leftarrow \hat{p}_i + c(n_i)$ ,  $\alpha'_i \leftarrow \alpha_i/p_i$ ,  $\delta'_i \leftarrow \delta_i - e^{-2n_i c^2(n_i)}$ ; // e.g.,  $c(n) = \frac{2}{\sqrt{n}}$ 
8   if  $n'_i \geq \log \delta'_i / \log(1 - \alpha'_i)$  and  $\alpha'_i < 1$  then
9      $k'_i \leftarrow \text{DeltaSearch}(n'_i, \alpha'_i, \delta'_i)$ 
10     $\bar{t}_i \leftarrow t'_{i(k'_i)}$ 
11  end
12 end
Output:  $\bar{t}_i$ 

```

$R_{1\star}(\phi) = P_1(\phi(X) \in \{2, 3\})$ and $R_{2\star}(\phi) = P_2(\phi(X) = 3)$, which need to be controlled at prespecified levels α_1, α_2 with tolerance levels δ_1, δ_2 , respectively. In addition, we wish to minimize the weighted sum of errors

$$\begin{aligned}
R^c(\phi) &= \mathbb{P}(\phi(X) \neq Y) - \pi_1 R_{1\star}(\phi) - \pi_2 R_{2\star}(\phi) \\
&= \pi_2 P_2(\phi(X) = 1) + \pi_3 [P_3(\phi(X) = 1) + P_3(\phi(X) = 2)]. \quad (10)
\end{aligned}$$

When $\mathcal{I} = 3$, our H-NP umbrella algorithm relies on two scoring functions $T_1, T_2 : \mathcal{X} \rightarrow \mathbb{R}$, which can be constructed by Eq (3) using the estimates $\widehat{\mathbb{P}}(Y = i \mid X)$ from any scoring-type classification method:

$$T_1(X) = \widehat{\mathbb{P}}(Y = 1 \mid X) \quad \text{and} \quad T_2(X) = \frac{\widehat{\mathbb{P}}(Y = 2 \mid X)}{\widehat{\mathbb{P}}(Y = 3 \mid X)}. \quad (11)$$

The H-NP classifier then takes the form

$$\widehat{\phi}(X) = \begin{cases} 1, & T_1(X) \geq t_1; \\ 2, & T_2(X) \geq t_2 \quad \text{and} \quad T_1(X) < t_1; \\ 3, & \text{otherwise.} \end{cases} \quad (12)$$

Here T_2 determines whether an observation belongs to class 2 or class 3, with a larger value indicating a higher probability for class 2. Applying Algorithm 2, we can find \bar{t}_1 such that any threshold $t_1 \leq \bar{t}_1$ will satisfy the high probability control on the first under-diagnosis error, that is $\mathbb{P}(R_{1\star}(\widehat{\phi}) > \alpha_1) = \mathbb{P}(P_1 [T_1(X) < t_1 | \bar{t}_1] > \alpha_1) \leq \delta_1$. Recall that the computation of \bar{t}_2 (and consequently t_2) depends on the choice of t_1 . Given a fixed t_1 , the high probability control on the second under-diagnosis errors is $\mathbb{P}(R_{2\star}(\widehat{\phi}) > \alpha_2) = \mathbb{P}(P_2 [T_1(X) < t_1, T_2(X) < t_2 | \bar{t}_2] > \alpha_2) \leq \delta_2$, where \bar{t}_2 is computed by Algorithm 2 so that any $t_2 \leq \bar{t}_2$ satisfies the constraint.

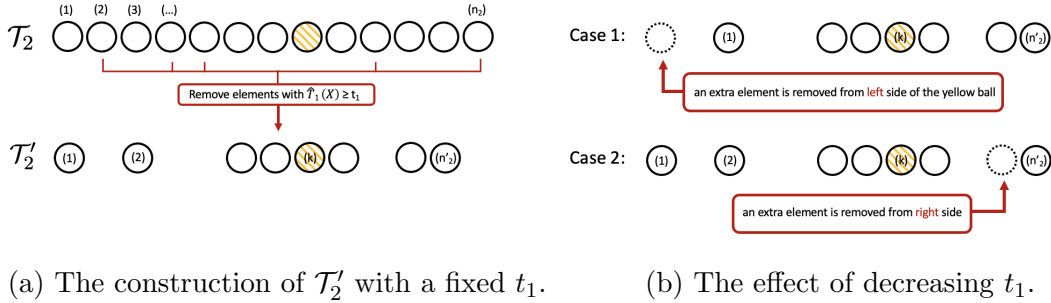


Figure 1: The influence of t_1 on the error $P_3(\widehat{Y} = 2)$.

The interaction between t_1 and t_2 comes into play when minimizing the remaining errors in $R^c(\widehat{\phi})$. First note that using Eq (10) and (12), the other types of errors in $R^c(\widehat{\phi})$ are

$$P_2(\widehat{\phi}(X) = 1) = P_2(T_1(X) \geq t_1), \quad P_3(\widehat{\phi}(X) = 1) = P_3(T_1(X) \geq t_1), \quad (13)$$

$$P_3(\widehat{\phi}(X) = 2) = P_3(T_1(X) < t_1, T_2(X) \geq t_2) .$$

To simplify the notation, let \widehat{Y} denote $\widehat{\phi}(X)$ in the following discussion. For a fixed t_1 , decreasing t_2 leads to an increase in $P_3(\widehat{Y} = 2)$ and has no effect on the other errors in (13), which means that $t_2 = \bar{t}_2$ minimizes $R^c(\widehat{\phi})$. However, the selection of t_1 is not as straightforward as t_2 . Figure 1a illustrates how the set $\mathcal{T}'_2 = \{T_2(X) \mid X \in \mathcal{S}_{2t}, T_1(X) < t_1\}$ (as appeared in Theorem 1) is constructed for a given t_1 , where the elements are ordered by their T_2 values. Clearly, more elements are removed from \mathcal{T}'_2 as t_1 decreases, leading to a smaller n'_2 . Consider an element in the set \mathcal{T}'_2 which has rank k in the ordered list (colored yellow in Figure 1a). Then k, n'_2, α'_2 , and consequently $v(k, n'_2, \alpha'_2)$, will all be affected by decreasing t_1 , but the change is not monotonic as shown in Figure 1b. Decreasing t_1 could remove elements (dashed circles in Figure 1b) either to the left side (case 1) or right side (case 2) of the yellow element, depending on the values of the scores T_1 . In case 1, $v(k, n'_2, \alpha'_2)$ decreases, resulting in a larger \bar{t}_2 and a smaller $P_3(\widehat{Y} = 2)$ error, whereas the reverse can happen in case 2. The details of how $v(k, n'_2, \alpha'_2)$ changes can be found in Supplementary Materials B.3, with additional simulations in Supplementary Figure S7. In view of the above, minimizing the empirical error \tilde{R}^c requires a grid search over t_1 , for which we use the set $\mathcal{T}_1 = \{T_1(X) \mid X \in \mathcal{S}_{1t}\}$, and the overall algorithm for finding the optimal thresholds and the resulting classifier is described in Algorithm 3, which we name as the H-NP umbrella algorithm.

2.4 Simulation studies

We first examine the validity of our H-NP umbrella algorithm using simulated data from **setting 1**: $\mathcal{I} = 3$, and the feature vectors in class i are generated as $(X^i)^\top \sim N(\mu_i, I)$,

Algorithm 3: H-NP umbrella algorithm for $\mathcal{I} = 3$

Input : Sample: $\mathcal{S} = \mathcal{S}_1 \cup \mathcal{S}_2 \cup \mathcal{S}_3$; levels: (α_1, α_2) ; tolerances: (δ_1, δ_2) ; grid set: A_1 (e.g., \mathcal{T}_1).

- 1 $\hat{\pi}_2 = |\mathcal{S}_2|/|\mathcal{S}|$; $\hat{\pi}_3 = |\mathcal{S}_3|/|\mathcal{S}|$
- 2 $\mathcal{S}_{1s}, \mathcal{S}_{1t} \leftarrow$ Random split \mathcal{S}_1 ;
- 3 $\mathcal{S}_{2s}, \mathcal{S}_{2t}, \mathcal{S}_{2e} \leftarrow$ Random split \mathcal{S}_2 ;
- 4 $\mathcal{S}_{3s}, \mathcal{S}_{3e} \leftarrow$ Random split \mathcal{S}_3
- 5 $\mathcal{S}_s = \mathcal{S}_{1s} \cup \mathcal{S}_{2s} \cup \mathcal{S}_{3s}$
- 6 $T_1, T_2 \leftarrow$ A base classification method(\mathcal{S}_s) ; // c.f. Eq (11)
- 7 $\bar{t}_1 \leftarrow$ UpperBound($\mathcal{S}_{1t}, \alpha_1, \delta_1, (T_1), \text{NULL}$)
- 8 $\tilde{R}^c = 1$
- 9 **for** $t_1 \in A_1 \cap (-\infty, \bar{t}_1]$ **do**
- 10 $t_2 \leftarrow$ UpperBound($\mathcal{S}_{2t}, \alpha_2, \delta_2, (T_1, T_2), (t_1)$) ; // i.e., Algorithm 2
- 11 $\hat{\phi} \leftarrow$ a classifier with respect to t_1, t_2
- 12 $\tilde{R}_{\text{new}}^c = (\hat{\pi}_2/|\mathcal{S}_{2e}|) \sum_{X \in \mathcal{S}_{2e}} \mathbb{1}\{\hat{\phi}(X) = 1\} + (\hat{\pi}_3/|\mathcal{S}_{3e}|) \sum_{X \in \mathcal{S}_{3e}} \mathbb{1}\{\hat{\phi}(X) \in \{1, 2\}\}$
- 13 **if** $\tilde{R}_{\text{new}}^c < \tilde{R}^c$ **then**
- 14 $\tilde{R}^c \leftarrow \tilde{R}_{\text{new}}^c, \hat{\phi}^* \leftarrow \hat{\phi}$
- 15 **end**
- 16 **end**

Output: $\hat{\phi}^*$

where $\mu_1 = (0, -1)^\top$, $\mu_2 = (-1, 1)^\top$, $\mu_3 = (1, 0)^\top$ and I is the 2×2 identity matrix. For each simulated dataset, we generate the feature vectors and labels with 500 observations in each of the three classes. The observations are randomly separated into parts for score training, threshold selection and computing empirical errors: \mathcal{S}_1 is split into 50%, 50% for $\mathcal{S}_{1s}, \mathcal{S}_{1t}$; \mathcal{S}_2 is split into 45%, 50% and 5% for $\mathcal{S}_{2s}, \mathcal{S}_{2t}$ and \mathcal{S}_{2e} ; \mathcal{S}_3 is split into 95%, 5% for $\mathcal{S}_{3s}, \mathcal{S}_{3e}$, respectively. All the results in this section are based on 1000 repetitions from a given setting. We set $\alpha_1 = \alpha_2 = 0.05$ and $\delta_1 = \delta_2 = 0.05$. To approximate and evaluate the true population errors $R_{1\star}, R_{2\star}$ and R^c , we additionally generate 20,000 observations for each class and refer to them as the test set.

First, we demonstrate that Algorithm 3 outputs an H-NP classifier with the desired high probability controls. More specifically, we show that any $t_1 \leq \bar{t}_1$ and $t_2 = \bar{t}_2$ (\bar{t}_1, \bar{t}_2 are computed by Algorithm 2) will lead to a valid threshold pair (t_1, t_2) satisfying $\mathbb{P}(R_{1\star}(\hat{\phi}) >$

$\alpha_1) \leq \delta_1$ and $\mathbb{P}(R_{2\star}(\hat{\phi}) > \alpha_2) \leq \delta_2$, where $R_{1\star}$ and $R_{2\star}$ are approximated using the test set in each round of simulation. Here, we use multinomial logistic regression to construct the scoring functions T_1 and T_2 , the inputs of Algorithm 3. Figure 2 displays the boxplots of various approximate errors with t_1 chosen as the k -th largest element in $\mathcal{T}_1 \cap (-\infty, \bar{t}_1]$ as k changes. In Figure 2a and 2b, where the blue diamonds mark the 95% quantiles, we can see that the violation rate of the required error bounds (red dashed lines, representing α_1 and α_2) is about 5% or less, suggesting our procedure provides effective controls on the errors of concerns. In this case, in most simulation rounds, \bar{t}_1 minimizes the empirical error \tilde{R}^c computed on \mathcal{S}_{2e} and \mathcal{S}_{3e} , and $t_1 = \bar{t}_1$ is chosen as the optimal threshold by Algorithm 3 in the final classifier. We can see this coincide with Figure 2c, which shows that the largest element in $\mathcal{T}_1 \cap (-\infty, \bar{t}_1]$ (i.e., \bar{t}_1) minimizes the approximate error R^c on the test set. We note here that the results from other split settings can be found in Supplementary Figures S5 and S6 and show similar trends. As the minimum sample size requirement on \mathcal{S}_{it} is 59 in this case, the setting in Figure 2 already exceeds the requirement. Further increasing its size makes minimal difference in the performance of the H-NP classifier.

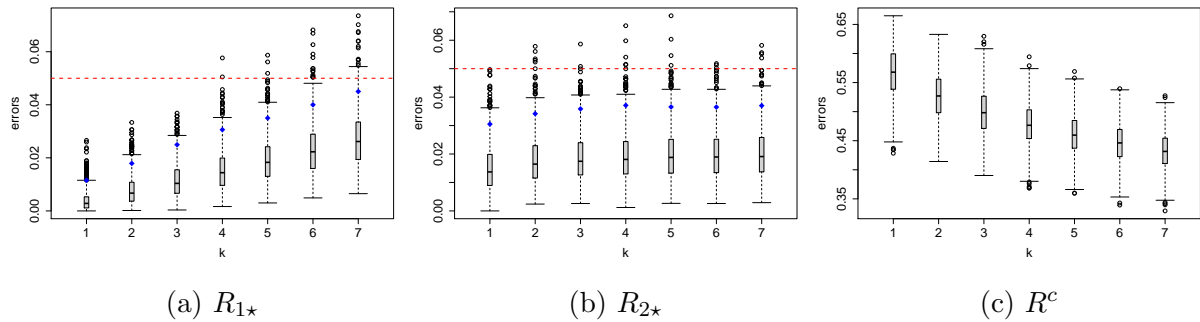
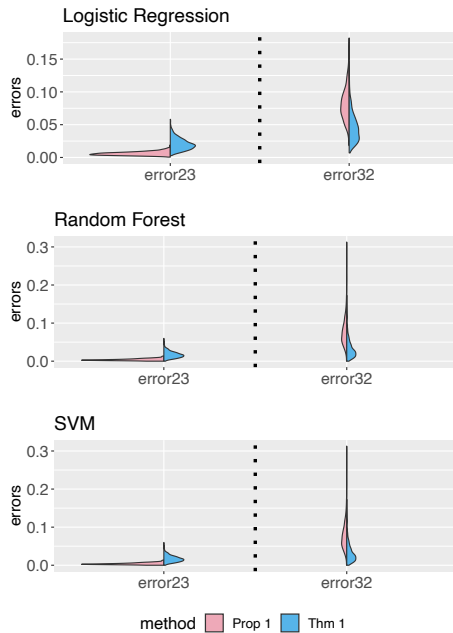


Figure 2: The distribution of approximate errors on the test set when t_1 is the k -th largest element in $\mathcal{T}_1 \cap (-\infty, \bar{t}_1]$. The 95% quantiles of $R_{1\star}$ and $R_{2\star}$ are marked by blue diamonds. The target control levels for $R_{1\star}(\hat{\phi})$ and $R_{2\star}(\hat{\phi})$ ($\alpha_1 = \alpha_2 = 0.05$) are plotted as red dashed lines.

Next, we check whether indeed Theorem 1 gives a better upper bound on t_2 than



Logistic Regression		
Method	Error23	Error32
Prop 1	0.006	0.082
Thm 1	0.020	0.046
Random Forest		
Method	Error23	Error32
Prop 1	0.004	0.077
Thm 1	0.017	0.033
SVM		
Method	Error23	Error32
Prop 1	0.004	0.077
Thm 1	0.018	0.033

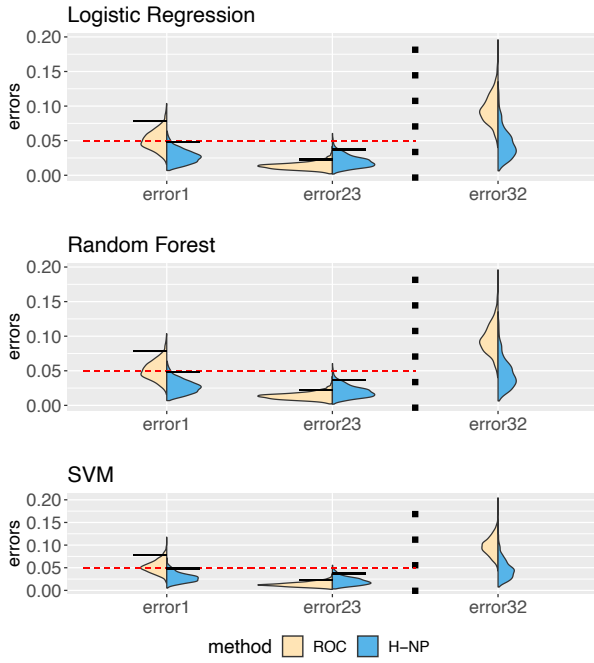
Figure 3: The distribution and averages of approximate errors on the test set under **setting 1**. “error23” and “error32” correspond to $R_{2\star}(\hat{\phi})$ and $P_3(\hat{Y} = 2)$, respectively.

Proposition 1 for overall error minimization. Recall the two upper bounds in Eq (6) ($t_{2(k_2)}$) and Eq (8) (\bar{t}_2). For each base classification algorithm (e.g., logistic regression), we set $t_1 = \bar{t}_1$ and t_2 equal to these two upper bounds respectively, resulting in two classifiers with different t_2 thresholds. We compare their performance by evaluating the approximate errors of $R_{2\star}(\hat{\phi})$ and $P_3(\hat{Y} = 2)$ since, as discussed in Section 2.3, the threshold t_2 only influences these two errors for a fixed t_1 . Figure 3 shows the distributions of the errors and also their averages for three different base classification algorithms. Under each algorithm, both choices of t_2 effectively control $R_{2\star}(\hat{\phi})$, but the upper bound from Proposition 1 is overly conservative compared with that of Theorem 1, which results in a notable increase in $P_3(\hat{Y} = 2)$. This is undesirable since $P_3(\hat{Y} = 2)$ is one component in $R^c(\hat{\phi})$, and the goal is to minimize $R^c(\hat{\phi})$ under appropriate error controls.

Now we consider comparing our H-NP classifier against alternative approaches. Since existing methods for controlling specific errors in the multi-class classification setting do not directly apply to the type of under-diagnosis errors we consider (e.g., Tian and Feng

[2021], Landgrebe and Duin [2005]) and provide “approximate” instead of high probability error controls, we construct an example of “approximate” error control using the empirical ROC curve approach. In this case, each class of observations is split into two parts: one for training the base classification method, the other for threshold selection using the ROC curve. Under **setting 1**, using similar split ratios as before, we separate \mathcal{S}_i into 50% and 50% for \mathcal{S}_{is} and \mathcal{S}_{it} for $i = 1, 2, 3$. The same test set is used. We re-compute the scoring functions (T_1 and T_2) corresponding to the new split. t_1 is selected using the ROC curve generated by T_1 aiming to distinguish between class 1 (samples in \mathcal{S}_{1t}) and class 2' (samples in $\mathcal{S}_{2t} \cup \mathcal{S}_{3t}$) merging classes 2 and 3, with specificity calculated as the rate of misclassifying a class-1 observation into class 2'. Similarly, t_2 is selected using T_2 dividing samples in $\mathcal{S}_{2t} \cup \mathcal{S}_{3t}$ into class 2 and class 3, with specificity defined as the rate of misclassifying a class-2 observation into class 3. More specifically, in Eq (12) we use $t_1 = \sup \left\{ t : \frac{\sum_{X \in \mathcal{S}_{1t}} \mathbf{1}\{T_1(X) < t\}}{|\mathcal{S}_{1t}|} \leq \alpha_1 \right\}$ and $t_2 = \sup \left\{ t : \frac{\sum_{X \in \mathcal{S}_{2t}} \mathbf{1}\{T_2(X) < t\}}{|\mathcal{S}_{2t}|} \leq \alpha_2 \right\}$ to obtain the classifier for the ROC curve approach.

The comparison between our H-NP classifier and the ROC curve approach is summarized in Figure 4. Recalling α_i and δ_i are both 0.05, we mark the 95% quantiles of the under-diagnosis errors by solid black lines and the target error control levels by dotted red lines. First we observe that the 95% quantiles of $R_{1\star}$ using the ROC curve approach well exceed the target level control, in fact with their averages centering around the target. We also see the influence of t_1 on the $R_{2\star}$ – without a suitable adjustment for t_2 based on t_1 , the control on $R_{2\star}(\hat{\phi})$ in the ROC curve approach is overly conservative despite it being an approximate error control method, which in turn leads to an inflation in the error $P_3(\hat{Y} = 2)$. In view of this, we further consider a simulation setting where the influence of t_1 on t_2 is smaller. **Setting 2** moves samples in class 1 further away from classes 2



Logistic Regression			
Method	Error1 (95% quantile)	Error23	Error32 (mean)
ROC	0.074	0.023	0.096
H-NP	0.045	0.036	0.047

Random Forest			
Method	Error1 (95% quantile)	Error23	Error32 (mean)
ROC	0.077	0.020	0.093
H-NP	0.047	0.034	0.032

SVM			
Method	Error1 (95% quantile)	Error23	Error32 (mean)
ROC	0.078	0.023	0.098
H-NP	0.048	0.037	0.047

Figure 4: The distributions of approximate errors on the test set under **setting 1**. “error1”, “error23” and “error32” correspond to $R_{1\star}(\hat{\phi})$, $R_{2\star}(\hat{\phi})$ and $P_3(\hat{Y} = 2)$, respectively.

and 3 by having $\mu_1 = (0, -3)^\top$, while the other parts remain the same as **setting 1**. The distributions of the under-diagnosis errors are shown in Figure 5, demonstrating that the ROC curve approach does not provide the required level of control for $R_{1\star}$ or $R_{2\star}$.

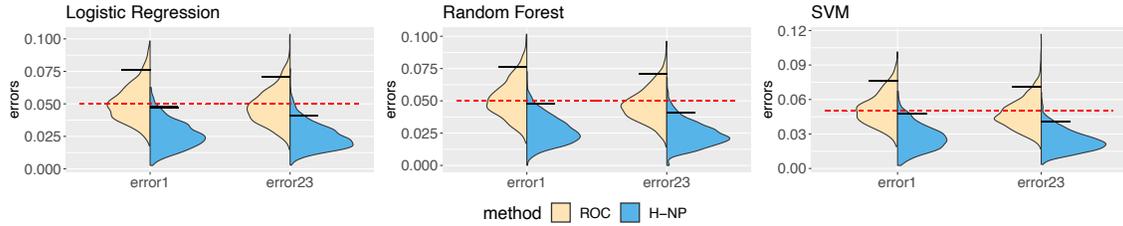


Figure 5: The distributions of approximate errors on the test set under **setting 2**. “error1” and “error23” correspond to the errors $R_{1\star}(\hat{\phi})$ and $R_{2\star}(\hat{\phi})$, respectively.

3 Application to COVID-19 severity classification

3.1 ScRNA-seq data and featurization

We integrate nine publicly available scRNA-seq datasets [Stephenson et al., 2021, Su et al., 2020, Schulte-Schrepping et al., 2020, Ren et al., 2021, Wilk et al., 2020, Liu et al., 2021, Arunachalam et al., 2020, Lee et al., 2020, Zhu et al., 2020] to form a total of 740 COVID-19 patients with three severity levels marked as “Severe” (212 patients), “Mild/Moderate” (387 patients), and “Healthy” (141 patients). The detail of each dataset and patient composition can be found in Supplementary Table S1. The severe, moderate and healthy patients are labeled as class 1, 2 and 3, respectively.

For each patient, PBMC scRNA-seq data is available in the form of a matrix recording the expression levels of genes in hundreds to thousands of cells. Following the workflow in Lin et al. [2020a], we first perform data integration including batch effect removal and cell type annotation, before selecting 3,000 highly variable genes and constructing their pseudo-bulk expression profiles under each cell type, where each gene’s expression is averaged across the cells of this type in every patient. The resulting processed data for each patient j is a matrix $A^{(j)} \in \mathbb{R}^{n_g \times n_c}$, where $n_c = 19$ is the number of cell types, and $n_g = 3,000$ is the number of genes for analysis. More details of the integration process can be found in Supplementary Materials A. Supplementary Figure S1 shows the distribution of the sparsity levels, i.e., the proportion of genes with zero values, under each cell type across all the patients. Further breaking each distribution into the three severity classes, Supplementary Figure S2 shows that, in some cell types (e.g., DC and CD16 Monocyte), the sparsity level, which to some extent indicates the activity level of the immune cell type, varies across the three classes and thus can be informative for classification. Since age information is available (although in different forms, see Supplementary Table S3) in most of the nine

datasets we integrate, we include it as an additional clinical variable for classification. The details of processing the age variable are deferred to Supplementary Materials [A](#).

Since classical classification methods typically use feature vectors as input, appropriate featurization that transforms the expression matrices into vectors is needed. We propose four ways of featurization that differ in their considerations of the following aspects.

- As we observe the sparsity level in some cell types changes across the severity classes, we expect different treatments of zeros will influence the classification performance. Three approaches are proposed: 1) no special treatment ([M.1](#)); 2) remove all the zeros ([M.3](#)); 3) remove cell types with significant amount of zeros across all three classes ([M.2](#) and [M.4](#)).
- Dimension reduction is commonly used to project the information in a matrix onto a vector. We consider performing dimension reduction along different directions, namely row projections, which take combinations of genes ([M.2](#)), and column projections, which combine cell types with appropriate weights ([M.3](#) and [M.4](#)). We aim to compare choices of projection direction, so we focus on principal component analysis (PCA) as our dimension reduction method.
- We consider two approaches to generate the PCA loadings: 1) overall PCA loadings ([M.2](#) and [M.3](#)), where we perform PCA on the whole data to output a loading vector for all patients; 2) patient-specific PCA loadings ([M.4](#)), where PCA is performed for each matrix $A^{(j)}$ to get an individual-specific loading vector.

The details of each featurization method are as follows.

M.1 Simple feature screening: we consider each element $A_{uv}^{(j)}$ (gene u under cell type v) as a possible feature for patient j and use its standard deviation across all patients,

denoted as SD_{uv} , to screen the features. Elements that hardly vary across the patients are likely to have a low discriminative power for classification. Let $SD_{(i)}$ be the i -th largest element in $\{SD_{uv} \mid u \in [n_g], v \in [n_c]\}$. The feature vector for each patient consists of the entries in $\{A_{uv}^{(j)} \mid SD_{uv} \geq SD_{(n_f)}\}$, where n_f is the number of features desired and set to 3,000.

M.2 Overall gene combination: removing cell types with mostly zero expression values across all patients (details in Supplementary Materials A), we select 16 cell types to construct $\tilde{A}^{(j)} \in \mathbb{R}^{n_g \times 16}$ that only preserves columns in $A^{(j)}$ corresponding to the selected cell types. Then, $\tilde{A}^{(1)}, \dots, \tilde{A}^{(N)}$ are concatenated column-wise to get $\tilde{A}^{\text{all}} \in \mathbb{R}^{n_g \times (N \times 16)}$, where $N = 740$. Let $\tilde{w} \in \mathbb{R}^{n_g \times 1}$ denote the first principle component loadings of $(\tilde{A}^{\text{all}})^\top$, and the feature vector for patient j is given by $X_j = \tilde{w}^\top \tilde{A}^{(j)}$.

M.3 Common cell type combination: we compute an expression matrix \bar{A} averaged over all patients defined as

$$\bar{A}_{uv} = \frac{\sum_{j \in [N]} A_{uv}^{(j)}}{|\{j \in [N] \mid A_{uv}^{(j)} \neq 0\}|},$$

where $|\cdot|$ is the cardinality function. Let $w \in \mathbb{R}^{n_c \times 1}$ denote the first principle component loadings of \bar{A} , then the feature vector for the j -th patient is $X_j = (A^{(j)}w)^\top$.

M.4 Individual-specific cell type combination: for patient j , the feature vector $X_j \in \mathbb{R}^{1 \times 16}$ is taken as the first principle component of $\tilde{A}^{(j)}$, the matrix with selected 16 cell types in M.2. Different from M.2 and M.3, the principle component loading vector \tilde{w}_j that produces $X_j = (\tilde{A}^{(j)}\tilde{w}_j)^\top$ is patient-specific, intending to reflect different cell type compositions in different individuals.

We next evaluate the performance of these featurizations when applied as input to

different base classification methods for H-NP classification.

3.2 Results of H-NP classification

After obtaining the feature vectors and applying a suitable base classification method, we apply Algorithm 3 to control the under-diagnosis errors. Recall that $Y = 1, 2, 3$ represent the severe, moderate and healthy categories, respectively, and the goal is to control $R_{1\star}(\hat{\phi})$ and $R_{2\star}(\hat{\phi})$. In this section, we evaluate the performance of the H-NP classifier applied to each combination of featurization method in Section 3.1 and base classification method (logistic regression, random forest, SVM (linear model)), which is used to train the scores (T_1 and T_2). In each class, we leave out 20% of the data as the test set and split the rest 80% as follows for training the H-NP classifier: 40% and 40% of \mathcal{S}_1 form \mathcal{S}_{1s} and \mathcal{S}_{1t} ; 40%, 30% and 10% of \mathcal{S}_2 form \mathcal{S}_{2s} , \mathcal{S}_{2t} and \mathcal{S}_{1e} ; 40% and 40% of \mathcal{S}_3 form \mathcal{S}_{3s} and \mathcal{S}_{3e} . For each combination of featurization and base classification method, we perform random splitting of the observations for 50 times to produce the results in this section.

In Figure 6, the yellow halves of the violin plots show the distributions of different approximate errors from the classical classification methods; Table 1 records the averages of these errors. In all the cases, the approximate error of $R_{1\star}$ is greater than 30%, in many cases greater than 50%, which can have serious implications for severe patients. Under the H-NP paradigm, we set $\alpha_1 = 0.2$ and $\delta_1 = 0.1$, i.e., we want to control the under-diagnosis error of the severe class under 20% at a 10% tolerance level. On the other hand, we observe that the approximate error $R_{2\star}$ under the classical paradigm is already relatively low, with the averages around 10%. In this case, we consider $\alpha_2 = 10\%$ and $\delta_2 = 10\%$, controlling the under-diagnosis error for the moderate class under 10% at a 10% tolerance level.

With the prespecified $\alpha_1, \alpha_2, \delta_1, \delta_2$, for a given base classification method Algorithm 3 outputs an H-NP classifier that controls the under-diagnosis errors while minimizing the

Logistic Regression							
Featurization	Paradigm	Error1	Error23	Error21	Error31	Error32	Overall
M.1	classical	0.362	0.107	0.182	0.083	0.250	0.319
	H-NP	0.128	0.044	0.451	0.429	0.229	0.420
M.2	classical	0.537	0.090	0.175	0.151	0.599	0.436
	H-NP	0.126	0.039	0.613	0.530	0.335	0.540
M.3	classical	0.352	0.105	0.147	0.056	0.254	0.292
	H-NP	0.129	0.039	0.453	0.346	0.266	0.410
M.4	classical	0.337	0.090	0.142	0.051	0.260	0.278
	H-NP	0.134	0.043	0.358	0.291	0.294	0.359

Random Forest							
Featurization	Paradigm	Error1	Error23	Error21	Error31	Error32	Overall
M.1	classical	0.469	0.031	0.087	0.057	0.477	0.298
	H-NP	0.126	0.045	0.464	0.410	0.168	0.412
M.2	classical	0.559	0.049	0.110	0.168	0.477	0.367
	H-NP	0.129	0.041	0.554	0.532	0.203	0.487
M.3	classical	0.514	0.027	0.092	0.074	0.534	0.327
	H-NP	0.138	0.045	0.437	0.361	0.200	0.397
M.4	classical	0.514	0.021	0.086	0.039	0.583	0.322
	H-NP	0.121	0.040	0.444	0.298	0.192	0.380

SVM							
Featurization	Paradigm	Error1	Error23	Error21	Error31	Error32	Overall
M.1	classical	0.395	0.076	0.146	0.060	0.248	0.288
	H-NP	0.129	0.045	0.447	0.210	0.303	0.390
M.2	classical	0.520	0.040	0.167	0.184	0.683	0.423
	H-NP	0.140	0.039	0.568	0.501	0.380	0.524
M.3	classical	0.350	0.056	0.118	0.037	0.241	0.245
	H-NP	0.125	0.042	0.392	0.132	0.230	0.331
M.4	classical	0.341	0.055	0.117	0.028	0.242	0.240
	H-NP	0.131	0.049	0.394	0.127	0.219	0.334

Table 1: The averages of approximate errors. “error1”, “error23”, “error21”, “error32”, “overall” correspond to $R_{1\star}(\hat{\phi})$, $R_{2\star}(\hat{\phi})$, $P_2(\hat{Y} = 1)$, $P_3(\hat{Y} = 1)$, $P_3(\hat{Y} = 2)$ and $P(\hat{Y} \neq Y)$, respectively.

weighted sum of the other empirical errors. The blue half violin plots in Figure 6 and Table 1 show the resulting approximate errors after H-NP adjustment. We observe that the individual-specific feature M.4 consistently leads to smaller errors under both the classical and H-NP classifiers, especially for linear classification models (logistic regression and SVM). We have also implemented a neural network classifier. However, as the training sample size is relatively small (40% of 740 patients), its performance is not as good as the linear classification models, and the results are deferred to Supplementary Figure S8.

In each plot of Figure 6, the two leftmost plots are the distributions of the two approx-

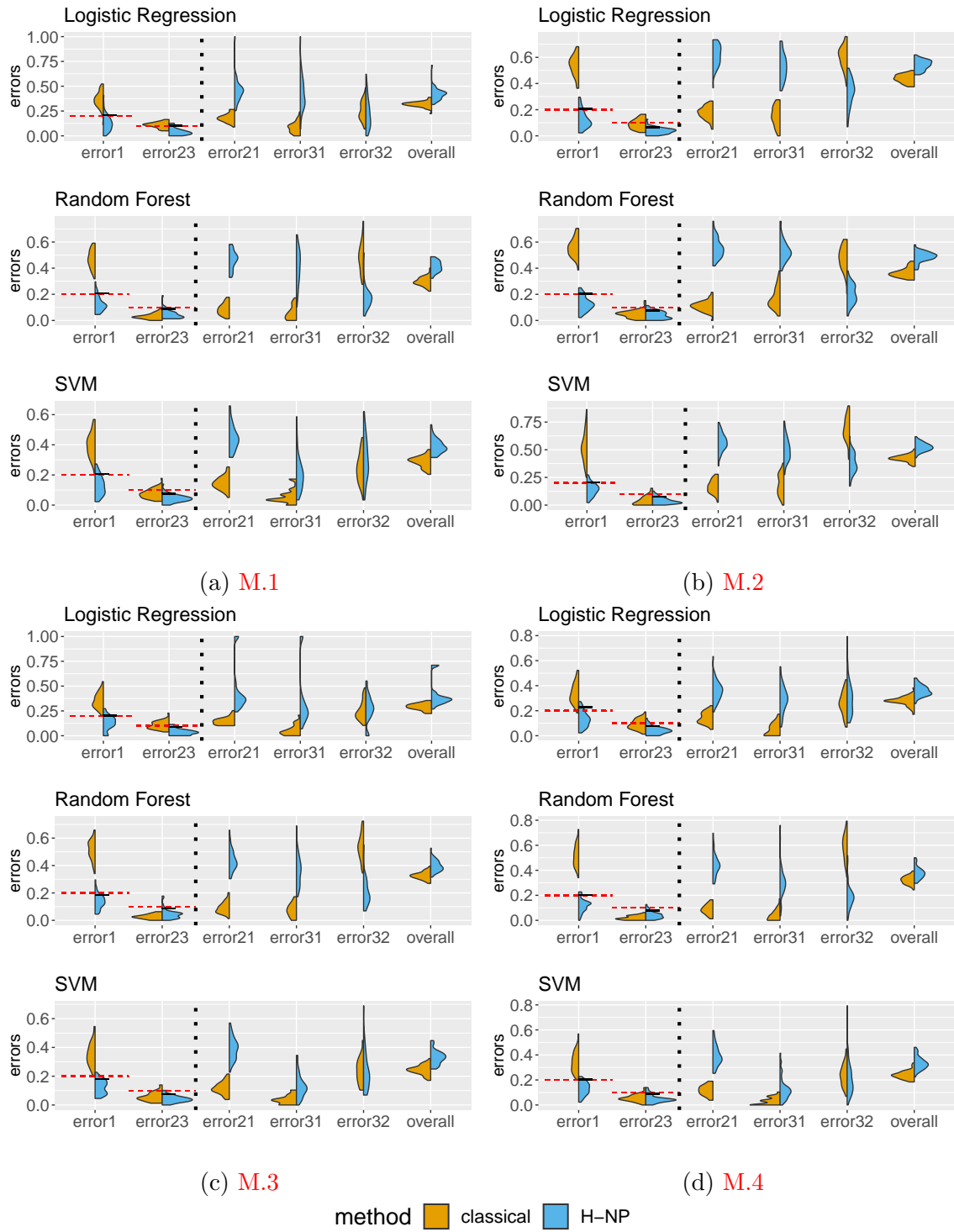


Figure 6: The distribution of approximate errors for each combination of featurization method and base classification method. “error1”, “error23”, “error21”, “error32”, “overall” correspond to $R_{1\star}(\hat{\phi})$, $R_{2\star}(\hat{\phi})$, $P_2(\hat{Y} = 1)$, $P_3(\hat{Y} = 1)$, $P_3(\hat{Y} = 2)$ and $P(\hat{Y} \neq Y)$, respectively.

imate under-diagnosis errors $R_{1\star}$ and $R_{2\star}$. We mark the 90% quantiles of $R_{1\star}$ and $R_{2\star}$ by short black lines (since $\delta_1 = \delta_2 = 0.1$), and the desired control levels ($\alpha_1 = 0.2$, $\alpha_2 = 0.1$) by red dashed lines. The four rightmost plots show the approximate errors for the overall risk and the three components in $R^c(\hat{\phi})$ as discussed in Eq (13). For all the featurizations and base classification methods, the under-diagnosis errors are controlled at the desired levels with an increment in the overall errors which is small compared to the reduction in under-diagnosis errors. This demonstrates consistency of our method and indicates its general applicability to various base classification algorithms chosen by users.

Another interesting phenomenon is that when a classical classification method is overly conservative for specified α_i and δ_i , our algorithm will increase the corresponding threshold t_i , which relaxes the decision boundary for classes less prioritized than i . As a result, the relaxation will benefit some components in $R^c(\hat{\phi})$. For example, in Figure 6d, the random forest classifier always produces the approximate error $R_{2\star}$ less than 0.1, which means it is too conservative for the control level $\alpha_2 = 0.1$ at the tolerance level $\delta_2 = 0.1$. In this case, the NP classifier adjusts the threshold t_2 to lower the requirement for class 3, thus significantly decreasing the approximate error of $P_3(\hat{Y} = 2)$. Similar observations can be made in Figures 6a–6c for the random forest classifier.

Finally, we take a closer look at the loading vectors $\{\tilde{w}_j\}_{j \in [N]}$ given by the individual-specific featurization M.4, which consistently gives the best performance under different classification algorithms. For visualization, we concatenate \tilde{w}_j^\top into a $16 \times N$ matrix W and plot its first two principal components comparing the severe class against the other two classes. Supplementary Figures S3a–S3b show that the severe class tends to have lower PC1 and higher PC2 values, suggesting the loading vectors have captured cell type weights containing information for characterizing severity levels. Further inspecting the biplot in

Figure S3c, one can see that the loading of CD8⁺ effector T cells has a large influence on both PCs, which is consistent with known involvement of CD8⁺ T cells in the immune response of severe patients [Diao et al., 2020, Stephenson et al., 2021].

4 Discussion

In disease severity classification, under-diagnosis errors are more consequential in the sense that they increase the risk of patients receiving insufficient medical care. By assuming the classes have a prioritized ordering, we propose an H-NP classification framework and its associated algorithm (Algorithm 3) capable of controlling under-diagnosis errors at desired levels with high probability. The algorithm performs post hoc adjustment on scoring-type classification methods and thus can be applied in conjunction with most methods preferred by users. Through simulation and the case study of COVID-19 severity classification, we demonstrate the efficacy of our algorithm in achieving the desired error controls. We have also compared different ways of constructing interpretable feature vectors from the multi-patient scRNA-seq data and shown that the individual-specific PCA featurization consistently achieves the best performance under various classification settings.

Even though our case study has three classes, the framework and algorithm developed are general. Increasing the number of classes has no effect on the minimum size requirement of the left-out part of each class for threshold selection, since it suffices for each class i to satisfy $n_i \geq \log \delta_i / (1 - \alpha_i)$. We also note that the notion of prioritized classes can be defined in a context-specific way. For example, in some diseases like Alzheimer’s disease, the transitional stage is considered to be the most important [Xiong et al., 2006].

There are several interesting directions for future work. For small data problems where the minimum sample size requirement is not full-filled, we might consider adopting a parametric model, under which we can not only develop a new algorithm without minimum

sample size requirement, but also study the oracle type properties of the classifiers. In terms of featurizing multi-patient scRNA-seq data, we have chosen PCA as the dimension reduction method to focus on other aspects of comparison; more dimension reduction methods can be explored in future work.

Acknowledgements

The authors would like to thank Dr Yingxin Lin and the Sydney Precision Bioinformatics Group for their generous help with curating and processing the COVID-19 scRNA-seq data.

References

- Rebecca A Betensky and Yang Feng. Accounting for incomplete testing in the estimation of epidemic parameters. *International journal of epidemiology*, 49(5):1419–1426, 2020.
- Corbin Quick, Rounak Dey, and Xihong Lin. Regression models for understanding covid-19 epidemic dynamics with incomplete data. *Journal of the American Statistical Association*, 116(536):1561–1577, 2021.
- Logan C Brooks, Evan L Ray, Jacob Bien, Johannes Bracher, Aaron Rumack, et al. Comparing ensemble approaches for short-term probabilistic covid-19 forecasts in the us. *International Institute of Forecasters*, 2020.
- Francesca Tang, Yang Feng, Hamza Chiheb, and Jianqing Fan. The interplay of demographic variables and social distancing scores in deep prediction of us covid-19 cases. *Journal of the American Statistical Association*, 116(534):492–506, 2021.
- Daniel J McDonald, Jacob Bien, Alden Green, Addison J Hu, Nat DeFries, et al. Can

auxiliary indicators improve covid-19 forecasting and hotspot prediction? *Proceedings of the National Academy of Sciences*, 118(51), 2021.

Nick James, Max Menzies, and Peter Radchenko. Covid-19 second wave mortality in europe and the united states. *Chaos: An Interdisciplinary Journal of Nonlinear Science*, 31(3): 031105, 2021.

Peter Kramlinger, Tatyana Krivobokova, and Stefan Sperlich. Marginal and conditional multiple inference for linear mixed model predictors. *Journal of the American Statistical Association*, 0(ja):1–31, 2022. doi: 10.1080/01621459.2022.2044826. URL <https://doi.org/10.1080/01621459.2022.2044826>.

Jiangpeng Wu, Pengyi Zhang, Liting Zhang, Wenbo Meng, Junfeng Li, et al. Rapid and accurate identification of covid-19 infection through machine learning based on clinical available blood test results. *MedRxiv*, 2020.

Wei Tse Li, Jiayan Ma, Neil Shende, Grant Castaneda, Jaideep Chakladar, et al. Using machine learning of clinical data to diagnose covid-19: a systematic review and meta-analysis. *BMC medical informatics and decision making*, 20(1):1–13, 2020.

Jiawei Zhang, Jie Ding, and Yuhong Yang. Is a classification procedure good enough?—a goodness-of-fit assessment tool for classification learning. *Journal of the American Statistical Association*, pages 1–11, 2021.

Li Yan, Hai-Tao Zhang, Yang Xiao, Maolin Wang, Chuan Sun, et al. Prediction of criticality in patients with severe covid-19 infection using three clinical features: a machine learning-based prognostic model with clinical data in wuhan. *MedRxiv*, 27:2020, 2020.

Liping Sun, Fengxiang Song, Nannan Shi, Fengjun Liu, Shenyang Li, et al. Combination of

four clinical indicators predicts the severe/critical symptom of patients infected covid-19. *Journal of Clinical Virology*, 128:104431, 2020.

Zirun Zhao, Anne Chen, Wei Hou, James M Graham, Haifang Li, et al. Prediction model and risk scores of icu admission and mortality in covid-19. *PloS one*, 15(7):e0236618, 2020.

Anthony Ortiz, Anusua Trivedi, Jocelyn Desbiens, Marian Blazes, Caleb Robinson, et al. Effective deep learning approaches for predicting covid-19 outcomes from chest computed tomography volumes. *Scientific reports*, 12(1):1–10, 2022.

Norah Alballa and Isra Al-Turaiki. Machine learning approaches in covid-19 diagnosis, mortality, and severity risk prediction: A review. *Informatics in Medicine Unlocked*, 24:100564, 2021.

Katherine A Overmyer, Evgenia Shishkova, Ian J Miller, Joseph Balnis, Matthew N Bernstein, et al. Large-scale multi-omic analysis of covid-19 severity. *Cell systems*, 12(1):23–40, 2021.

Aaron J Wilk, Arjun Rustagi, Nancy Q Zhao, Jonasel Roque, Giovanny J Martínez-Colón, et al. A single-cell atlas of the peripheral immune response in patients with severe covid-19. *Nature medicine*, 26(7):1070–1076, 2020.

Emily Stephenson, Gary Reynolds, Rachel A Botting, Fernando J Calero-Nieto, Michael D Morgan, et al. Single-cell multi-omics analysis of the immune response in covid-19. *Nature medicine*, 27(5):904–916, 2021.

Xianwen Ren, Wen Wen, Xiaoying Fan, Wenhong Hou, Bin Su, et al. Covid-19 immune

- features revealed by a large-scale single-cell transcriptome atlas. *Cell*, 184(7):1895–1913, 2021.
- World Health Organization. Who r&d blueprint novel coronavirus covid-19 therapeutic trial synopsis. *World Health Organization*, pages 1–9, 2020.
- Xin Tong, Yang Feng, and Jingyi Jessica Li. Neyman-pearson classification algorithms and np receiver operating characteristics. *Science advances*, 4(2):eaao1659, 2018.
- Yingxin Lin, Lipin Loo, Andy Tran, Cesar Moreno, Daniel Hesselson, et al. Characterization of cell-cell communication in covid-19 patients. *bioRxiv*, 2020a.
- Klemens B Meyer and Stephen G Pauker. Screening for hiv: can we afford the false positive rate?, 1987.
- Marcel Dettling and Peter Bühlmann. Boosting for tumor classification with gene expression data. *Bioinformatics*, 19(9):1061–1069, 2003.
- Adam Cannon, James Howse, Don Hush, and Clint Scovel. Learning with the neyman-pearson and min-max criteria. *Los Alamos National Laboratory, Tech. Rep. LA-UR*, pages 02–2951, 2002.
- Clayton Scott and Robert Nowak. A neyman-pearson approach to statistical learning. *IEEE Transactions on Information Theory*, 51(11):3806–3819, 2005.
- Philippe Rigollet and Xin Tong. Neyman-pearson classification, convexity and stochastic constraints. *Journal of Machine Learning Research*, 2011.
- Lucy Xia, Richard Zhao, Yanhui Wu, and Xin Tong. Intentional control of type i error over unconscious data distortion: A neyman-pearson approach to text classification. *Journal of the American Statistical Association*, 116(533):68–81, 2021.

Yang Feng, Xin Tong, and Weining Xin. Targeted crisis risk control: A neyman-pearson approach. *Available at SSRN 3945980*, 2021.

Thomas Landgrebe and R Duin. On neyman-pearson optimisation for multiclass classifiers. In *Proceedings 16th Annual Symposium of the Pattern Recognition Association of South Africa. PRASA*, pages 165–170, 2005.

Chengjie Xiong, Gerald van Belle, J Philip Miller, and John C Morris. Measuring and estimating diagnostic accuracy when there are three ordinal diagnostic groups. *Statistics in medicine*, 25(7):1251–1273, 2006.

Ye Tian and Yang Feng. Neyman-pearson multi-class classification via cost-sensitive learning. *arXiv preprint arXiv:2111.04597*, 2021.

Natalie Stanley, Ina A Stelzer, Amy S Tsai, Ramin Fallahzadeh, Edward Ganio, et al. Vopo leverages cellular heterogeneity for predictive modeling of single-cell data. *Nature communications*, 11(1):1–9, 2020.

Edward A Ganio, Natalie Stanley, Viktoria Lindberg-Larsen, Jakob Einhaus, Amy S Tsai, et al. Preferential inhibition of adaptive immune system dynamics by glucocorticoids in patients after acute surgical trauma. *Nature communications*, 11(1):1–12, 2020.

Xiaoyuan Han, Mohammad S Ghaemi, Kazuo Ando, Laura S Peterson, Edward A Ganio, et al. Differential dynamics of the maternal immune system in healthy pregnancy and preeclampsia. *Frontiers in immunology*, page 1305, 2019.

Mark M Davis, Cristina M Tato, and David Furman. Systems immunology: just getting started. *Nature immunology*, 18(7):725–732, 2017.

Yapeng Su, Daniel Chen, Dan Yuan, Christopher Lausted, Jongchan Choi, et al. Multi-omics resolves a sharp disease-state shift between mild and moderate covid-19. *Cell*, 183(6):1479–1495, 2020.

Jonas Schulte-Schrepping, Nico Reusch, Daniela Paclik, Kevin Baßler, Stephan Schlickeiser, et al. Severe covid-19 is marked by a dysregulated myeloid cell compartment. *Cell*, 182(6):1419–1440, 2020.

Can Liu, Andrew J Martins, William W Lau, Nicholas Rachmaninoff, Jinguo Chen, et al. Time-resolved systems immunology reveals a late juncture linked to fatal covid-19. *Cell*, 184(7):1836–1857, 2021.

Prabhu S Arunachalam, Florian Wimmers, Chris Ka Pun Mok, Ranawaka APM Perera, Madeleine Scott, et al. Systems biological assessment of immunity to mild versus severe covid-19 infection in humans. *Science*, 369(6508):1210–1220, 2020.

Jeong Seok Lee, Seongwan Park, Hye Won Jeong, Jin Young Ahn, Seong Jin Choi, et al. Immunophenotyping of covid-19 and influenza highlights the role of type i interferons in development of severe covid-19. *Science immunology*, 5(49):eabd1554, 2020.

Linnan Zhu, Penghui Yang, Yingze Zhao, Zhenkun Zhuang, Zhifeng Wang, et al. Single-cell sequencing of peripheral mononuclear cells reveals distinct immune response landscapes of covid-19 and influenza patients. *Immunity*, 53(3):685–696, 2020.

Bo Diao, Chenhui Wang, Yingjun Tan, Xiewan Chen, Ying Liu, et al. Reduction and functional exhaustion of t cells in patients with coronavirus disease 2019 (covid-19). *Frontiers in immunology*, page 827, 2020.

Davis J McCarthy, Kieran R Campbell, Aaron TL Lun, and Quin F Wills. Scater: pre-

processing, quality control, normalization and visualization of single-cell rna-seq data in r. *Bioinformatics*, 33(8):1179–1186, 2017.

Yingxin Lin, Shila Ghazanfar, Kevin YX Wang, Johann A Gagnon-Bartsch, Kitty K Lo, et al. scmerge leverages factor analysis, stable expression, and pseudoreplication to merge multiple single-cell rna-seq datasets. *Proceedings of the National Academy of Sciences*, 116(20):9775–9784, 2019.

Yingxin Lin, Yue Cao, Hani Jieun Kim, Agus Salim, Terence P Speed, et al. scclassify: sample size estimation and multiscale classification of cells using single and multiple reference. *Molecular systems biology*, 16(6):e9389, 2020b.

Aaron TL Lun, Davis J McCarthy, and John C Marioni. A step-by-step workflow for low-level analysis of single-cell rna-seq data with bioconductor. *F1000Research*, 5, 2016.

Marmar Moussa and Ion I Măndoiu. Single cell rna-seq data clustering using tf-idf based methods. *BMC genomics*, 19(6):31–45, 2018.

Supplementary Materials

A Preprocessing of the integrated COVID-19 data

We integrate nine collections of scRNA-seq datasets from peripheral blood mononuclear cells (PBMCs). A total of 740 patients are available and their severity levels can be found in Table S1. We note that some of these datasets contain patients with longitudinal records of severity levels; we take the severity level on the day that their scRNA-seq sample was collected.

Before integration, we performed size factor standardization and log transformation on the raw count expression matrices using the `logNormCount` function in the R package `scater` (version 1.16.2) [McCarthy et al., 2017] and generated log transformed gene expression matrices. The nine PBMC datasets are integrated by a modified version of `scMerge` [Lin et al., 2019]. To construct pseudo-bulk expression profiles, we input the cell types annotated by `scClassify` [Lin et al., 2020b] (using cell types in Stephenson et al. [2021] as reference) into `scMerge`. The resulting profiles are used to identify mutual nearest subgroups as pseudo-replicates and to estimate parameters of the `scMerge` model. We select the top 3,000 highly variable genes through the function `modelGeneVar` in R package `scrn` [Lun et al., 2016], and for each patient calculate the average expression of each cell type for selected genes, i.e., for each patient, the integrated dataset provides a $n_g \times n_c$ matrix recording the average gene expressions, where n_g is the number of genes ($n_g = 3,000$) and n_c is the number of cell types ($n_c = 19$).

In the featurization methods M.2 and M.4, we remove cell types with its zero proportion hardly changing across all three classes (Figure S2) and an average zero proportion greater than 95% (Table S2). 16 cell types are left: B, CD14 Monocyte, CD16 Monocyte, CD4m

Publication	Severe	Mild/Moderate	Healthy	Total
Stephenson et al. [2021]	27	64	24	115
Su et al. [2020]	49	204	17	270
Schulte-Schrepping et al. [2020]	25	33	36	94
Ren et al. [2021]	36	43	28	107
Wilk et al. [2020]	15	15	10	40
Liu et al. [2021]	50	4	14	68
Arunachalam et al. [2020]	4	3	5	12
Lee et al. [2020]	6	5	4	15
Zhu et al. [2020]	0	16	3	19
Total	212	387	141	740

Table S1: Number of patients under each severity level in each dataset.

T, CD4n T, CD8eff T, CD8m T, DC, IgA PB, IgG PB, Neutrophil, NK, pDC, Platelet, RBC, SC & Eosinophil.

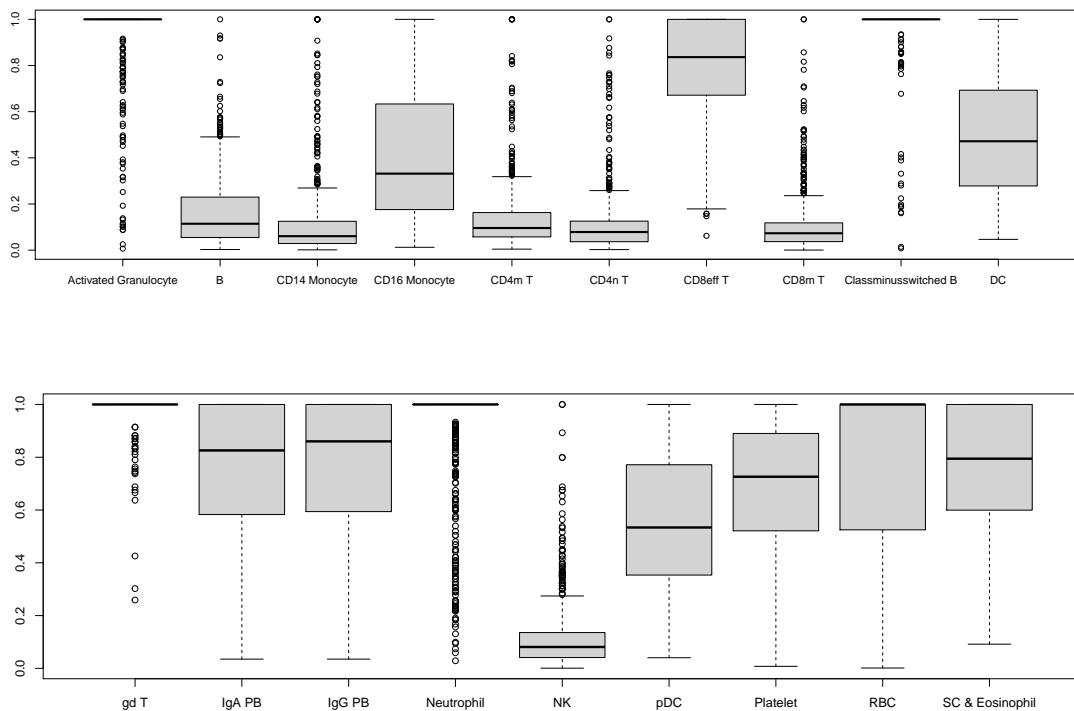


Figure S1: The distribution of the proportion of zero values across patients for each cell type.

Other than scRNA-seq data, we also include age as a predictor in the integrated dataset. Seven of the datasets used in our study recorded age information either as an exact number or an age group, while two datasets did not provide this information (see Table S3). In

cell type	zero proportion	cell type	zero proportion
Activated Granulocyte	0.961	gd T	0.991
B	0.164	IgA PB	0.749
CD14 Monocyte	0.113	IgG PB	0.769
CD16 Monocyte	0.427	Neutrophil	0.923
T	0.138	NK	0.116
CD4n T	0.111	pDC	0.566
CD8eff T	0.803	Platelet	0.691
CD8m T	0.105	RBC	0.779
Classminusswitched B	0.981	SC Eosinophil	0.752
DC	0.500		

Table S2: The average proportion of zero values across patients for each cell type.

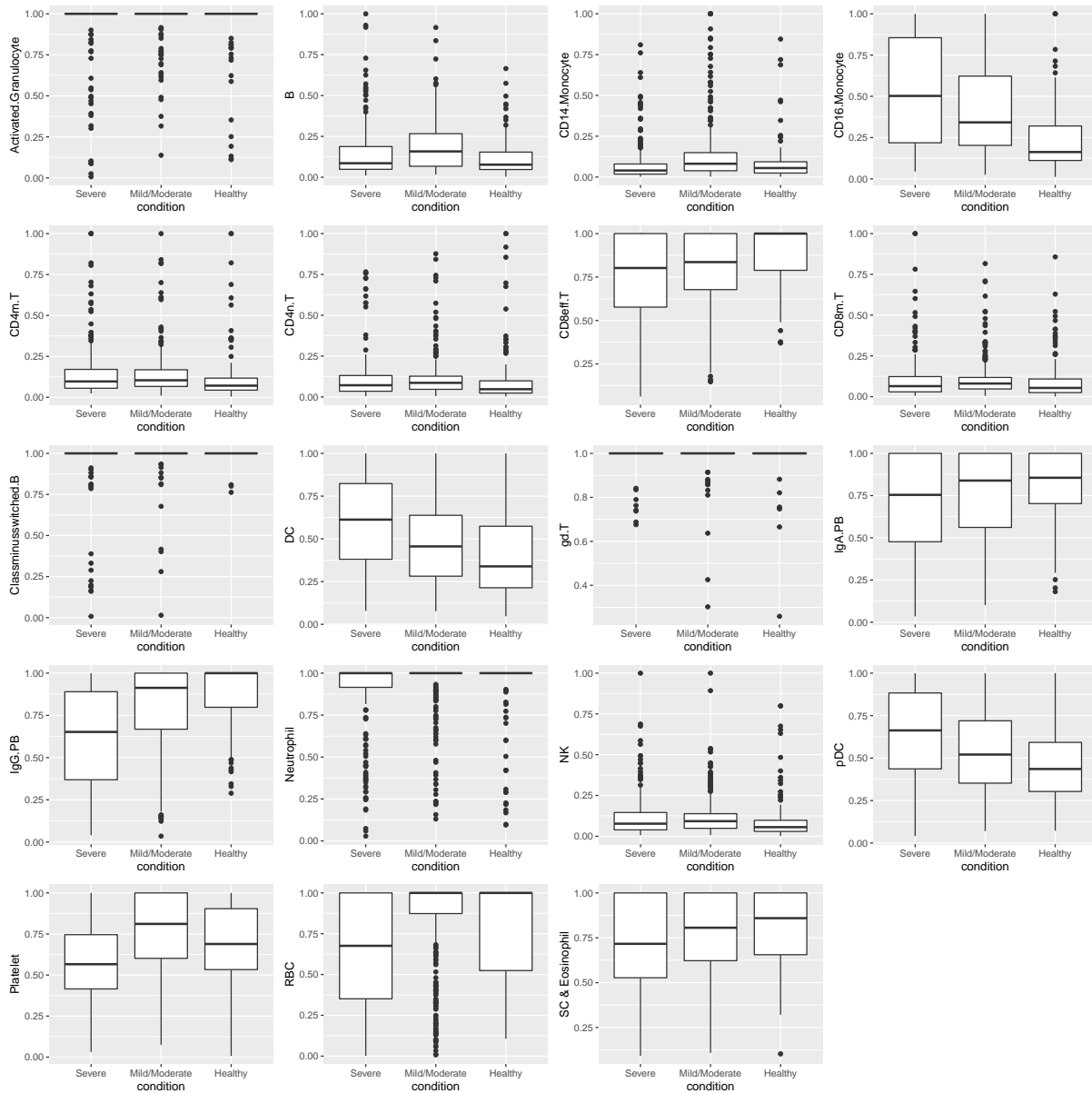


Figure S2: The proportions of zeros for different severity classes.

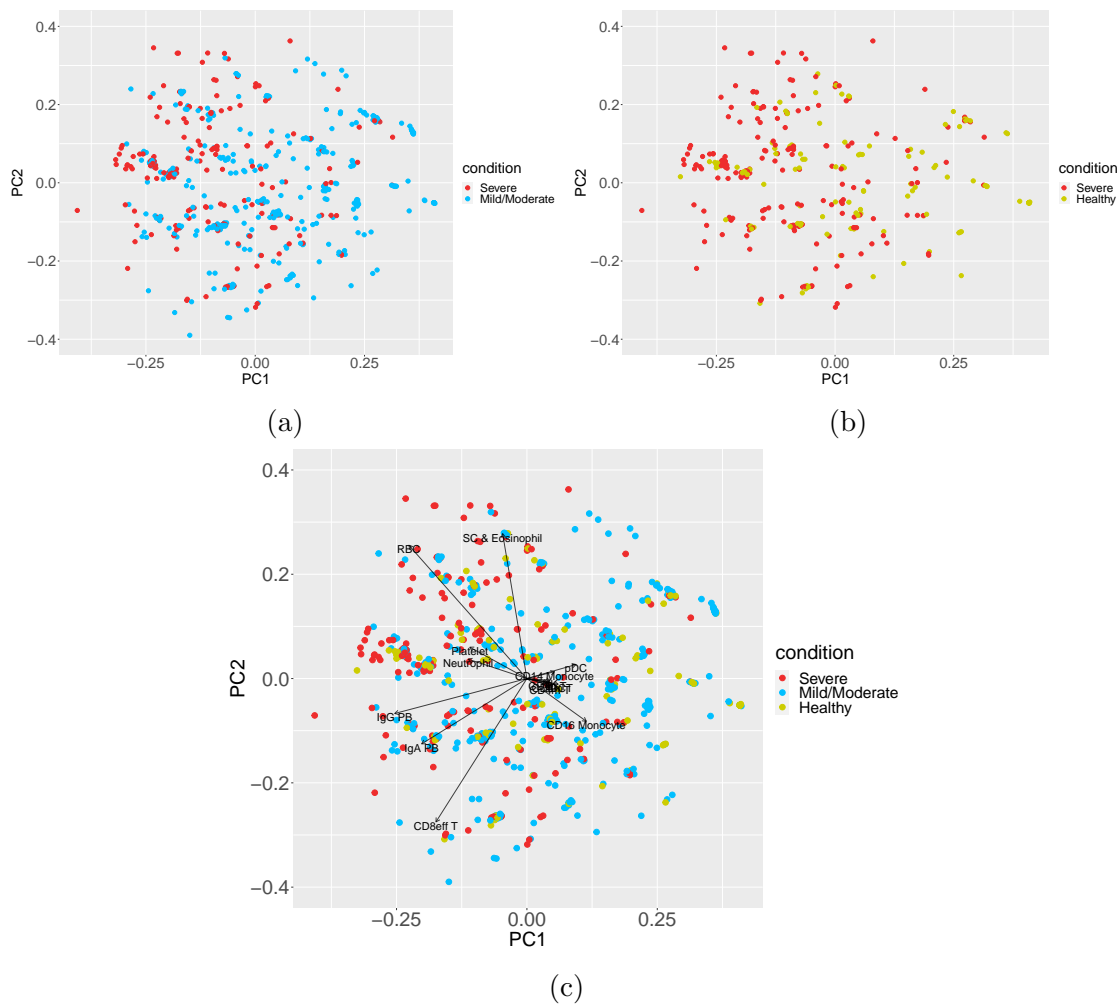


Figure S3: The first two PCs and loading plot of the weight matrix W used in M.4.

the integrated dataset, we use the lower end of the age group recorded for patients with no exact age, and replace the missing values with the average age (53.93).

Publication	Age recording format	Example
Stephenson et al. [2021]	age group	60-69
Su et al. [2020]	exact age	64
Schulte-Schrepping et al. [2020]	age group	61-65
Ren et al. [2021]	exact age	64
Wilk et al. [2020]	age group	60-69
Liu et al. [2021]	exact age	64
Arunachalam et al. [2020]	exact age	64
Lee et al. [2020]	not available	NA
Zhu et al. [2020]	not available	NA

Table S3: Format of age information in each dataset. An example record for a 64-year-old patient is provided for each dataset.

B Proofs of the main results

B.1 Proof of Proposition 1

Recall that $\mathcal{T}_i = \{T_i(X) \mid X \in \mathcal{S}_{it}\}$, and $t_{i(1)}, \dots, t_{i(n_i)}$ are the order statistics, with n_i being the cardinality of \mathcal{T}_i . Let $t_{i(k)}$ be the k -th order statistic. Suppose $T_i(X)$ is the classification score of an independent observation from class i , and F_i is the cumulative distribution function for $-T_i(X)$. Then,

$$P_i [T_i(X) < t_{i(k)} \mid t_{i(k)}] = P_i [-T_i(X) > -t_{i(k)} \mid t_{i(k)}] = 1 - F_i(-t_{i(k)}),$$

and

$$\begin{aligned} & \mathbb{P} (P_i [T_i(X) < t_{i(k)} \mid t_{i(k)}] > \alpha) \\ &= \mathbb{P} [1 - F_i(-t_{i(k)}) > \alpha] = \mathbb{P} [-t_{i(k)} < F_i^{-1}(1 - \alpha)] \\ &= \mathbb{P} [-t_{i(k)} < F_i^{-1}(1 - \alpha), -t_{i(k+1)} < F_i^{-1}(1 - \alpha), \dots, -t_{i(n_i)} < F_i^{-1}(1 - \alpha)] \\ &= \mathbb{P} [\text{at least } n_i - k + 1 \text{ elements in } \mathcal{T}_i \text{ are less than } F_i^{-1}(1 - \alpha)] \\ &= \sum_{j=n_i-k+1}^{n_i} \binom{n_i}{j} \mathbb{P} [-T_i(X) < F_i^{-1}(1 - \alpha)]^j (1 - \mathbb{P} [-T_i(X) < F_i^{-1}(1 - \alpha)])^{n_i-j} \\ &= \sum_{j=0}^{k-1} \binom{n_i}{j} (1 - \mathbb{P} [-T_i(X) < F_i^{-1}(1 - \alpha)])^j \mathbb{P} [-T_i(X) < F_i^{-1}(1 - \alpha)]^{n_i-j} \\ &= (n_i + 1 - k) \binom{n_i}{k-1} \int_0^{\mathbb{P}[-T_i(X) < F_i^{-1}(1-\alpha)]} u^{n_i-k} (1-u)^{k-1} du \\ &\leq (n_i + 1 - k) \binom{n_i}{k-1} \int_0^{1-\alpha} u^{n_i-k} (1-u)^{k-1} du \\ &= \sum_{j=0}^{k-1} \binom{n_i}{j} (\alpha)^j (1 - \alpha)^{n_i-j} = v(k, n_i, \alpha) \end{aligned} \tag{S.1}$$

The inequality holds because $\mathbb{P}[-T_i(X) < F_i^{-1}(1 - \alpha)] \leq 1 - \alpha$, and it becomes an equality when F_i is continuous.

B.2 Proof of Theorem 1

Given $(t_1, t_2, \dots, t_{i-1})$, recall that $t_{i(k)}$ and $t'_{i(k)}$ are the k -th order statistic of the sets

$$\mathcal{T}_i = \{T_i(X) \mid X \in \mathcal{S}_{it}\} \quad \text{and} \quad \mathcal{T}'_i = \{T_i(X) \mid X \in \mathcal{S}_{it}, T_1(X) < t_1, \dots, T_{i-1}(X) < t_{i-1}\},$$

respectively, where \mathcal{S}_{it} is the left-out class- i samples, and $(t_1, t_2, \dots, t_{i-1})$ are the thresholds for the previous decisions in the classifier (3). n_i and n'_i are the cardinalities of \mathcal{T}_i and \mathcal{T}'_i .

Obviously, $n'_i \leq n_i$. Also, we set

$$\hat{p}_i = \frac{n'_i}{n_i}, \quad p_i = \hat{p}_i + c(n_i), \quad \alpha'_i = \frac{\alpha_i}{p_i}, \quad \delta'_i = \delta_i - \exp\{-2n_i c^2(n_i)\},$$

where α_i and δ_i are the prespecified control level and violation tolerance level, α'_i and δ'_i are the adjusted counterparts, and $c(n) = \mathcal{O}(1/\sqrt{n})$. With the adjusted α'_i and δ'_i , we consider the following two cases when selecting the upper bound of threshold:

$$\bar{t}_i = \begin{cases} t'_{i(k'_i)}, & \text{if } n'_i \geq \log \delta'_i / \log(1 - \alpha'_i) \quad \text{and} \quad \alpha'_i < 1; \\ t_{i(k_i)}, & \text{otherwise,} \end{cases} \quad (\text{S.2})$$

where $k_i = \max\{k \mid v(k, n_i, \alpha_i) \leq \delta_i\}$ and $k'_i = \max\{k \mid v(k, n'_i, \alpha'_i) \leq \delta'_i\}$. We are going to prove that $\mathbb{P}(P_i [T_1(X) < t_1, \dots, T_{i-1}(X) < t_{i-1}, \quad \text{and} \quad T_i(X) < \bar{t}_i \mid \bar{t}_i] > \alpha_i) \leq \delta_i$ by two cases.

Case 1: We consider the set $\mathcal{E} = \{n'_i \geq \log \delta'_i / \log(1 - \alpha'_i) \quad \text{and} \quad 1 - \alpha'_i > 0\}$ (case 1

in Eq (S.2)). Under this event, and we want to show that

$$\mathbb{P} \left(P_i \left[T_1(X) < t_1, \dots, T_{i-1}(X) < t_{i-1}, \quad \text{and} \quad T_i(X) < t'_{i(k'_i)} \middle| t'_{i(k'_i)} \right] > \alpha_i \middle| \mathcal{E} \right) \leq \delta_i.$$

Suppose that $T_i(X)$ is the classification score of an independent observation from class i . F'_i is the cumulative distribution function for the classification score $-T_i(X)$ when $T_1(X) < t_1, \dots, T_{i-1}(X) < t_{i-1}$. Then, similar to the proof of Proposition 1,

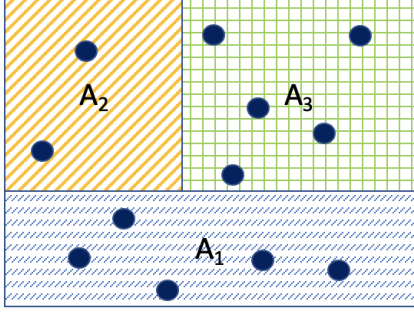
$$P_i \left[T_i(X) < t'_{i(k)} \middle| t'_{i(k)}, T_1(X) < t_1, \dots, T_{i-1}(X) < t_{i-1} \right] = 1 - F'_i \left(-t'_{i(k)} \right).$$

Note that α'_i is determined by n_i, n'_i, α_i . Meanwhile, δ'_i is fixed, as it only depends on the given values n_i and δ_i . We have

$$\begin{aligned} & \mathbb{P} \left(P_i \left[T_i(X) < t'_{i(k)} \middle| t'_{i(k)}, T_1(X) < t_1, \dots, T_{i-1}(X) < t_{i-1} \right] > \alpha'_i \middle| n'_i \right) \\ &= \mathbb{P} \left[-t'_{i(k)} > (F'_i)^{-1}(1 - \alpha'_i) \middle| n'_i \right] \\ &= \frac{\mathbb{P} \left[-t'_{i(k)} > (F'_i)^{-1}(1 - \alpha'_i) \quad \text{and} \quad |\mathcal{T}_i| = n'_i \right]}{\mathbb{P}(|\mathcal{T}_i| = n'_i)} \end{aligned} \quad (\text{S.3})$$

Note that the event $\{-t'_{i(k)} > (F'_i)^{-1}(1 - \alpha'_i) \quad \text{and} \quad |\mathcal{T}_i| = n'_i\}$ indicates that n'_i elements in \mathcal{S}_{it} satisfy $\{T_1(X) < t_1, \dots, T_{i-1}(X) < t_{i-1}\}$; among these elements, at least $n'_i - k + 1$ elements have $T_i(X)$ less than $(F'_i)^{-1}(1 - \alpha'_i)$. We can consider \mathcal{S}_{it} as independent draws from a multinomial distribution with three kinds of outcomes (A_1, A_2, A_3) defined in Supplementary Figure S4. Therefore,

$$\mathbb{P} \left[-t'_{i(k)} > (F'_i)^{-1}(1 - \alpha'_i) \quad \text{and} \quad |\mathcal{T}_i| = n'_i \right]$$



- \mathbf{A}_1 : $T_j(X) \geq t_j$ for some $j \in [i-1]$
 \mathbf{A}_2 : $T_j(X) < t_j$ for all $j \in [i-1]$, and $T_i(X) \geq (F'_i)^{-1}(1 - \alpha'_i)$
 \mathbf{A}_3 : $T_j(X) < t_j$ for all $j \in [i-1]$, and $T_i(X) < (F'_i)^{-1}(1 - \alpha'_i)$
 \bullet : the elements in \mathcal{S}_{it}

Figure S4: Partition of \mathcal{S}_{it} into three kinds of outcomes.

$$\begin{aligned}
&= \sum_{j=n'_i-k+1}^{n'_i} \binom{n_i}{n_i - n'_i, n'_i - j, j} P_i(A_1)^{n_i - n'_i} P_i(A_2)^{n'_i - j} P_i(A_3)^j; \\
&\mathbb{P}(|\mathcal{T}_i| = n'_i) \\
&= \binom{n_i}{n_i - n'_i} P_i(A_1)^{n_i - n'_i} P_i(A_2 \cup A_3)^{n'_i}.
\end{aligned}$$

Then, by Eq (S.3),

$$\begin{aligned}
&\mathbb{P} \left(P_i \left[T_i(X) < t'_{i(k)} \mid t'_{i(k)}, T_1(X) < t_1, \dots, T_{i-1}(X) < t_{i-1} \right] > \alpha'_i \mid n'_i \right) \\
&= \sum_{j=n'_i-k+1}^{n'_i} \binom{n'_i}{j} \left(\frac{P_i(A_2)}{P_i(A_2 \cup A_3)} \right)^{n'_i - j} \left(\frac{P_i(A_3)}{P_i(A_2 \cup A_3)} \right)^j \\
&= \sum_{j=n'_i-k+1}^{n'_i} \binom{n'_i}{j} (1 - P_i[-T_i(X) < (F'_i)^{-1}(1 - \alpha) \mid T_1(X) < t_1, \dots, T_{i-1}(X) < t_{i-1}])^{n'_i - j} \\
&\quad \times P_i[-T_i(X) < (F'_i)^{-1}(1 - \alpha'_i) \mid T_1(X) < t_1, \dots, T_{i-1}(X) < t_{i-1}]^j \\
&= \sum_{j=0}^{k-1} \binom{n'_i}{j} (1 - P_i[-T_i(X) < (F'_i)^{-1}(1 - \alpha) \mid T_1(X) < t_1, \dots, T_{i-1}(X) < t_{i-1}])^j \\
&\quad \times P_i[-T_i(X) < (F'_i)^{-1}(1 - \alpha'_i) \mid T_1(X) < t_1, \dots, T_{i-1}(X) < t_{i-1}]^{n'_i - j} \\
&\leq \sum_{j=0}^{k-1} \binom{n'_i}{j} (\alpha'_i)^j (1 - \alpha'_i)^{n'_i - j} = v(k, n'_i, \alpha'_i).
\end{aligned}$$

The last inequality holds because

$$P_i \left[-T_i(X) < (F'_i)^{-1}(1 - \alpha'_i) \mid T_1(X) < t_1, \dots, T_{i-1}(X) < t_{i-1} \right] \leq 1 - \alpha'_i,$$

and it becomes an equality when $(F'_i)^{-1}$ is continuous.

Also,

$$\mathbb{P} \left(P_i \left[T_i(X) < t'_{i(k'_i)} \mid t'_{i(k'_i)}, T_1(X) < t_1, \dots, T_{i-1}(X) < t_{i-1} \right] > \alpha'_i \mid n'_i \right) \leq \delta'_i$$

since $k'_i = \max\{k \mid v(k, n'_i, \alpha'_i) \leq \delta'_i\}$. Then,

$$\begin{aligned} & \mathbb{P} \left(P_i \left[T_i(X) < t'_{i(k'_i)} \mid t'_{i(k'_i)}, T_1(X) < t_1, \dots, T_{i-1}(X) < t_{i-1} \right] > \alpha'_i \mid \mathcal{E} \right) \\ &= \mathbb{E} \left[\sum_{j=0}^{k'_i-1} \binom{n'_i}{j} (\alpha'_i)^j (1 - \alpha'_i)^{n'_i-j} \mid \mathcal{E} \right] \\ &\leq \mathbb{E}[\delta'_i \mid \mathcal{E}] = \delta'_i. \end{aligned} \tag{S.4}$$

On the other hand, note that the event $\mathcal{E} = \{\alpha'_i < 1 \text{ and } n'_i \geq \log \delta'_i / \log(1 - \alpha'_i)\}$ is equivalent to

$$\left(1 - \frac{\alpha_i n_i}{n'_i + n_i c(n_i)} \right)^{n'_i} \leq \delta'_i \tag{S.5}$$

and

$$\frac{\alpha_i n_i}{n'_i + n_i c(n_i)} < 1. \tag{S.6}$$

The left part of the inequality (S.6) is decreasing with respect to n'_i . Also, the left part of the inequality (S.5) is nonincreasing in n'_i when the inequality (S.6) holds, which implies

that

$$\mathbb{E}[n'_i \mid n'_i \geq \log \delta'_i \log(1 - \alpha'_i) \text{ and } \alpha'_i < 1] \geq \mathbb{E}[n'_i \mid n'_i < \log \delta'_i / \log(1 - \alpha'_i) \text{ or } \alpha'_i \geq 1],$$

i.e., $E[n'_i \mid \mathcal{E}] \geq E[n'_i \mid \mathcal{E}^c]$. Immediately,

$$P_i(T_1(X) < t_1, \dots, T_{i-1}(X) < t_{i-1}) = \mathbb{E} \left[\frac{n'_i}{n_i} \right] \leq \mathbb{E} \left[\frac{n'_i}{n_i} \mid \mathcal{E} \right] = \mathbb{E}[\hat{p}_i \mid \mathcal{E}],$$

so

$$\begin{aligned} & \mathbb{P}(P_i(T_1(X) < t_1, \dots, T_{i-1}(X) < t_{i-1}) > p_i \mid \mathcal{E}) \\ &= \mathbb{P}(P_i(T_1(X) < t_1, \dots, T_{i-1}(X) < t_{i-1}) - \hat{p}_i > c(n_i) \mid \mathcal{E}) \\ &\leq \mathbb{P}(\mathbb{E}[\hat{p}_i \mid \mathcal{E}] - \hat{p}_i > c(n_i) \mid \mathcal{E}) \\ &= \mathbb{P} \left(\mathbb{E} \left[\frac{n'_i}{n_i} \mid \mathcal{E} \right] - \frac{n'_i}{n_i} > c(n_i) \mid \mathcal{E} \right) \\ &= \mathbb{P}(\mathbb{E}[n'_i \mid \mathcal{E}] - n'_i > n_i c(n_i) \mid \mathcal{E}) \\ &\leq e^{-2n_i c^2(n_i)}. \end{aligned}$$

The last inequality is by Hoeffding's inequality. Then,

$$\begin{aligned} & \mathbb{P}(P_i(T_1(X) < t_1, \dots, T_{i-1}(X) < t_{i-1}, \text{ and } T_i(X) < t'_{i(k'_i)} \mid t'_{i(k'_i)}) > \alpha_i \mid \mathcal{E}) \\ &= \mathbb{P} \left[P_i(T_i(X) < t'_{i(k'_i)} \mid t'_{i(k'_i)}, T_1(X) < t_1, \dots, T_{i-1}(X) < t_{i-1}) \right. \\ &\quad \left. \times P_i(T_1(X) < t_1, \dots, T_{i-1}(X) < t_{i-1}) > \alpha_i \mid \mathcal{E} \right] \\ &\leq \mathbb{P}[P_i(T_i(X) < t'_{i(k'_i)} \mid t'_{i(k'_i)}, T_1(X) < t_1, \dots, T_{i-1}(X) < t_{i-1}) > \alpha_i / p_i \mid \mathcal{E}] \\ &\quad + \mathbb{P}[P_i(T_1(X) < t_1, \dots, T_{i-1}(X) < t_{i-1}) > p_i \mid \mathcal{E}] \end{aligned}$$

$$\leq \delta'_i + e^{-2n_i c^2(n_i)} = \delta_i, \quad (\text{S.7})$$

Case 2: We consider the event $\mathcal{E}^c = \{n'_i < \log \delta'_i / \log(1 - \alpha'_i) \text{ or } 1 - \alpha'_i \leq 0\}$. Under this event, $\bar{t}_i = t_{i(k_i)}$. Since n_i is deterministic, we have

$$\mathbb{P} \left(P_i [T_i(X) < t_{i(k)} \mid t_{i(k)}] > \alpha_i \mid \mathcal{E}^c \right) \leq \sum_{j=0}^{k-1} \binom{n_i}{j} (\alpha_i)^j (1 - \alpha_i)^{n_i - j} = v(k, n_i, \alpha_i).$$

The proof is similar to that of Eq (S.1) and (S.4), and even easier since n_i is deterministic.

We do not repeat the argument here. Recall that $k_i = \max\{k \mid v(k, n_i, \alpha_i) \leq \delta_i\}$, so

$$\begin{aligned} \mathbb{P} \left(P_i [T_1(X) < t_1, \dots, T_{i-1}(X) < t_{i-1}, \text{ and } T_i(X) < t_{i(k_i)} \mid t_{i(k_i)}] > \alpha_i \mid \mathcal{E}^c \right) \\ \leq \mathbb{P} \left(P_i [T_i(X) < t_{i(k_i)} \mid t_{i(k_i)}] > \alpha_i \mid \mathcal{E}^c \right) \leq \delta_i. \end{aligned} \quad (\text{S.8})$$

Eq (S.8) implies

By Eq (S.2), (S.7) and (S.8),

$$\mathbb{P} \left(P_i [T_1(X) < t_1, \dots, T_{i-1}(X) < t_{i-1}, \text{ and } T_i(X) < \bar{t}_i \mid \bar{t}_i] > \alpha_i \right) \leq \delta_i,$$

which implies the inequality (9) in Theorem 1.

B.3 The change of $v(k, n'_2, \alpha'_2)$ in Figure 1b

In the end of Section 2.3, we discuss the selection of t_1 and t_2 to minimize R^c . Recall that k denotes the position of yellow ball (in \mathcal{T}'_2) in Figure 1b; α'_2 and δ'_2 are the adjusted control level and violation tolerance for the second under-diagnosis error $R_{2\star}(\hat{\phi})$; n'_2 is the cardinality of \mathcal{T}'_2 . k , α'_2 and n'_2 are functions of t_1 . In the following discussion, we will show

that the change in $v(k, n'_2, \alpha'_2)$ with respect to changing t_1 is not monotonic.

We consider a random variable $Z \sim \text{Binomial}(n, \alpha)$. We abbreviate $P_{n,\alpha}(z) = P_{n,\alpha}(Z = z)$ and $F_{n,\alpha}(z) = P_{n,\alpha}(Z \leq z)$. Note that $F_{n,\alpha}(z) = v(z, n, \alpha)$. We will explore how the change of n (i.e., the change of n'_2) affect the value of $F_{n,\alpha}(z)$. The following lemma discusses the changes in case 1 of Figure 1b.

Lemma 1. *Let $Z \sim \text{Binomial}(n, \alpha_n)$, where $\alpha_n = \frac{c_1}{n+c_2}$ for some positive constant c_1 and c_2 , then $F_{n,\alpha_n}(z-1) < F_{n+1,\alpha_{n+1}}(z)$.*

Proof. Let $Y = Z + X$, where $Z \sim \text{Binomial}(n, \alpha)$ and $X \sim \text{Bernoulli}(\alpha)$ are independent.

Then, $Y \sim \text{Binomial}(n+1, \alpha)$ and

$$\begin{aligned}
F_{n+1,\alpha}(z) &= P(Y \leq z) = P(X + Z \leq z) \\
&= P(X \leq 1 \mid Z \leq z-1)P(Z \leq z-1) + P(X = 0 \mid Z = z)P(Z = z) \\
&= P(X \leq 1)F_{n,\alpha}(z-1) + P(X = 0)P_{n,\alpha}(z) \\
&= F_{n,\alpha}(z-1) + (1-\alpha)P_{n,\alpha}(z).
\end{aligned} \tag{S.9}$$

Also, for fixed z and n , we have

$$\begin{aligned}
\frac{dF_{n,\alpha}(z)}{d\alpha} &= \frac{d}{d\alpha}(n-z) \binom{n}{z} \int_0^{1-\alpha} u^{n-z-1}(1-u)^z du \\
&= -(n-z) \binom{n}{z} \alpha^z (1-\alpha)^{n-z-1} = -nP_{n-1,\alpha}(z).
\end{aligned}$$

Therefore, there exists a constant $c \in [\alpha_{n+1}, \alpha_n]$ such that

$$\frac{F_{n,\alpha_{n+1}}(z) - F_{n,\alpha_n}(z)}{\alpha_n - \alpha_{n+1}} = nP_{n-1,c}(z). \tag{S.10}$$

Note that $\alpha_n - \alpha_{n+1} > 0$. Then,

$$\begin{aligned}
& F_{n+1, \alpha_{n+1}}(z) - F_{n, \alpha_n}(z-1) \\
&= F_{n+1, \alpha_{n+1}}(z) - F_{n, \alpha_{n+1}}(z-1) + F_{n, \alpha_{n+1}}(z-1) - F_{n, \alpha_n}(z-1) \\
&\geq (1 - \alpha_{n+1})P_{n, \alpha_{n+1}}(z) > 0.
\end{aligned}$$

□

Note that

$$\alpha'_2 = \frac{\alpha_2}{p_2} = \frac{\alpha_2}{n'_2/n_2 + c(n_2)} = \frac{\alpha_2 n_2}{n'_2 + c(n_2)n_2}.$$

Since n_2 is fixed, we can write α_2 in the form of $\frac{c_1}{n'_2 + c_2}$ for some positive constants c_1 and c_2 . In other words, if we remove an element to the left of the yellow element in Figure 1b case 1, the value of $v(k, n'_2, \alpha'_2)$ will decrease.

By contrast, there are situations in case 2 of Figure 1b that will increase $v(k, n'_2, \alpha'_2)$, as discussed in the following lemma.

Lemma 2. *Let $Z \sim \text{Binomial}(n, \alpha_n)$, where $\alpha_n = \frac{c_1}{n+c_2}$ and $c_2 \geq c_1 > 0$. Fix $z > 0$, $F_{n, \alpha_n}(z)$ is decreasing with respect to $n \geq n_l$ where $n_l = \min\{n \mid (n-1)\alpha_{n+1} \geq z\}$.*

Proof. Eq (S.9) implies

$$F_{n+1, \alpha}(z) - F_{n, \alpha}(z) = -\alpha P_{n, \alpha}(z). \tag{S.11}$$

On the other hand, for fixed n and z ,

$$\frac{d \log(P_{n,\alpha}(z))}{d\alpha} = \frac{z}{\alpha} - \frac{n-z}{1-\alpha} \begin{cases} > 0, & \alpha < z/n; \\ = 0, & \alpha = z/n; \\ < 0, & \alpha > z/n, \end{cases} \quad (\text{S.12})$$

so $P_{n-1,c}(z)$ is decreasing on $[\alpha_{n+1}, \alpha_n]$ when $(n-1)\alpha_{n+1} \geq z$. Then, according to Eq (S.10)

$$F_{n,\alpha_{n+1}}(z) - F_{n,\alpha_n}(z) \leq n(\alpha_n - \alpha_{n+1})P_{n-1,\alpha_{n+1}}(z). \quad (\text{S.13})$$

By Eq (S.11) and (S.13), for $(n-1)\alpha_{n+1} \geq z$,

$$\begin{aligned} F_{n+1,\alpha_{n+1}}(z) - F_{n,\alpha_n}(z) &= F_{n+1,\alpha_{n+1}}(z) - F_{n,\alpha_{n+1}}(z) + F_{n,\alpha_{n+1}}(z) - F_{n,\alpha_n}(z) \\ &\leq -\alpha_{n+1}P_{n,\alpha_{n+1}}(z) + n(\alpha_n - \alpha_{n+1})P_{n-1,\alpha_{n+1}}(z) \\ &= -\binom{n}{z}(\alpha_{n+1})^{z+1}(1-\alpha_{n+1})^{n-z} \\ &\quad + \frac{n}{n+c_2} \binom{n-1}{z}(\alpha_{n+1})^{z+1}(1-\alpha_{n+1})^{n-z-1} \\ &= \left(\alpha_{n+1} - 1 + \frac{n-z}{n+c_2}\right) \binom{n}{z}(\alpha_{n+1})^{z+1}(1-\alpha_{n+1})^{n-z-1} \\ &\leq \left(-\frac{n+1+c_2-c_1}{n+1+c_2} + \frac{n}{n+c_2}\right) \binom{n}{z}(\alpha_{n+1})^{z+1}(1-\alpha_{n+1})^{n-z-1} \\ &= -\frac{(c_2-c_1)(n+c_2)+c_2}{(n+c_2)(n+c_2+1)} \binom{n}{z}(\alpha_{n+1})^{z+1}(1-\alpha_{n+1})^{n-z-1} \\ &< 0, \end{aligned}$$

since $c_2 \geq c_1 > 0$.

Futhermore,

$$(n-1)\alpha_{n+1} = \frac{n-1}{n+1+c_2}c_1$$

is increasing in n , i.e, any $n \geq n_l$ satisfies $(n - 1)\alpha_{n+1} \geq z$. It establishes that $F_{n,\alpha_n}(z)$ is decreasing with respect to n when $n \geq n_l$. \square

This lemma presents a situation for case 2 in Figure 1b, where $v(k, n'_2, \alpha'_2)$ will increase.

C Additional results for simulation studies

C.1 Additional plots for simulation studies in Section 2.4

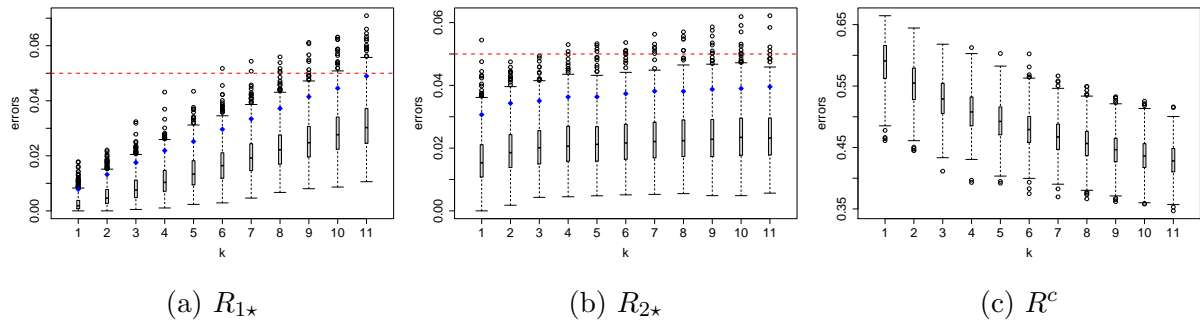


Figure S5: The distribution of approximate errors when t_1 is the k -th largest element in $\mathcal{T}_1 \cap (-\infty, \bar{t}_1)$. The 95% quantiles of R_{1*} and R_{2*} are marked by blue diamonds. The target control levels for $R_{1*}(\hat{\phi})$ and $R_{2*}(\hat{\phi})$ ($\alpha_1 = \alpha_2 = 0.05$) are plotted as red dashed lines. The data are generated under **setting 1** in Section 2.4 except a different sample splitting ratio is used: samples in \mathcal{S}_1 are randomly split into 30% for \mathcal{S}_{1s} (score), 70% for \mathcal{S}_{1t} (threshold); \mathcal{S}_2 are split into 25% for \mathcal{S}_{2s} , 70% for \mathcal{S}_{2t} , 5% for \mathcal{S}_{2e} (evaluation); \mathcal{S}_3 are split into 95% for \mathcal{S}_{3s} and 5% for \mathcal{S}_{3e} .

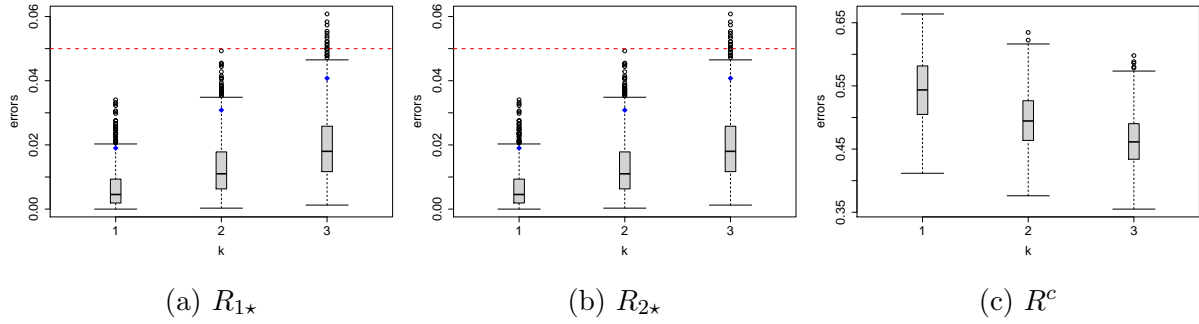
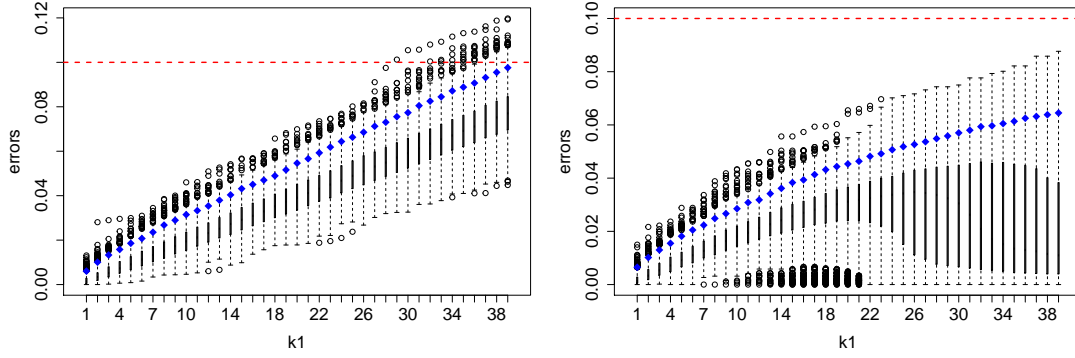


Figure S6: The distribution of approximate errors when t_1 is the k -th largest element in $\mathcal{T}_1 \cap (-\infty, \bar{t}_1)$. The 95% quantiles of R_{1*} and R_{2*} are marked by blue diamonds. The target control levels for $R_{1*}(\hat{\phi})$ and $R_{2*}(\hat{\phi})$ ($\alpha_1 = \alpha_2 = 0.05$) are plotted as red dashed lines. The data are generated under **setting 1** in Section 2.4 except a different sample splitting ratio is used: samples in \mathcal{S}_1 are randomly split into 70% for \mathcal{S}_{1s} , 30% for \mathcal{S}_{1t} ; \mathcal{S}_2 are split into 65% for \mathcal{S}_{2s} , 30% for \mathcal{S}_{2t} , 5% for \mathcal{S}_{2e} ; \mathcal{S}_3 are split into 95% for \mathcal{S}_{3s} and 5% for \mathcal{S}_{3e} .

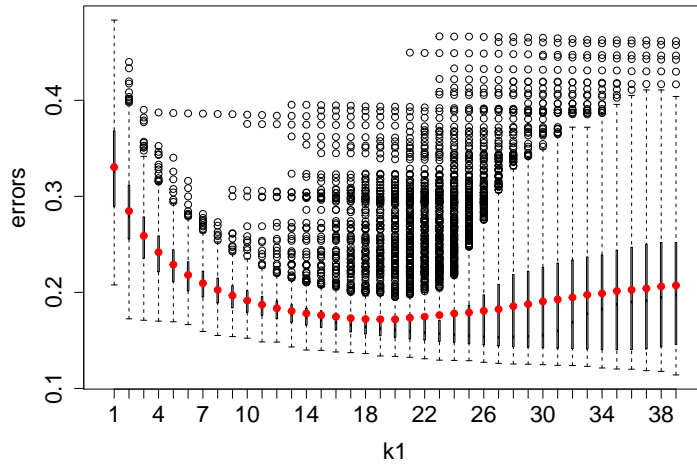
C.2 Additional simulation studies

We provide a simulation example to exhibit that the influence of t_1 on the weighted sum of errors $R^c(\hat{\phi})$ is not monotonic. The cause of the non-monotonicity is explained at the end of Section 2.3. Different from the simulations in Section 2.4, we adjust the proportion of each class by setting $n_1 = 1000, n_2 = 200, n_3 = 800$. As a result, the weight for $P_3(\hat{Y} \in \{1, 2\})$ in $R^c(\hat{\phi})$ increases, and the weight for $P_2(\hat{Y} = 1)$ decreases. We set $\mu_1 = (0, 0)^\top$, $\mu_2 = (-0.5, 0.5)^\top$, and $\mu_3 = (2, 2)^\top$. Under this setting, class 1 and 2 are closer in Euclidean distance compared to class 3. We increase α_1 and α_2 to 0.1 to get a wider search region for t_1 so that the pattern of R^c is easier to observe. To approximate the true errors R_{1*}, R_{2*} and R^c on a test set, we generate 30,000, 6,000 and 2,4000 observations for class 1, 2, 3, respectively. The ratio of the three classes in the test set is the same as $n_1 : n_2 : n_3$. Other settings are the same as **setting 1** in Section 2.4. The results of this new simulation setting are presented in Figure S7. We can observe that R^c is not monotonically decreasing, but our procedure still maintains effective controls on the under-diagnosis errors.



(a) $R_{1\star}$

(b) $R_{2\star}$

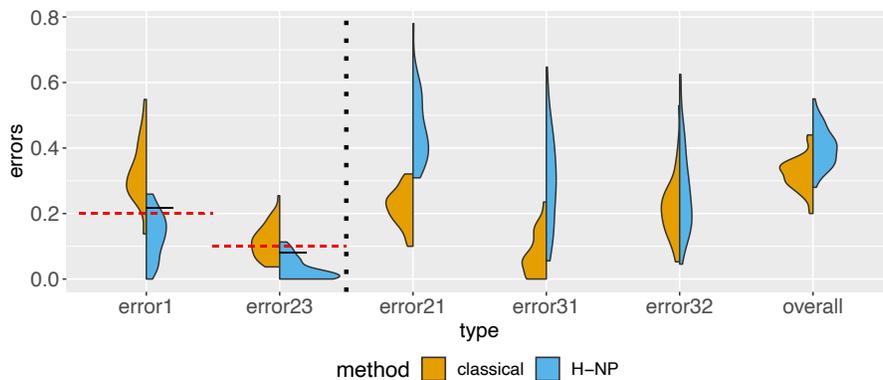


(c) R^c

Figure S7: The distribution of approximate errors when t_1 is the k -th largest element in $\mathcal{T}_1 \cap (-\infty, \bar{t}_1)$. The 95% quantiles ($\delta_1 = \delta_2 = 0.05$) of $R_{1\star}$ and $R_{2\star}$ are marked by blue diamonds. The target control levels for $R_{1\star}(\hat{\phi})$ and $R_{2\star}(\hat{\phi})$ ($\alpha_1 = \alpha_2 = 0.1$) are plotted as red dashed lines. Also, the averages of the R^c are marked by red points in (c).

D Additional results for COVID-19 severity classification

We apply the Term Frequency - Inverse Document Frequency (TF-IDF) transformation [Moussa and Măndoiu, 2018] to the matrix $(\tilde{A}^{(1)}, \dots, \tilde{A}^{(N)}) \in \mathbb{R}^{n_g \times (16 \times N)}$, and let the vector $A_{\text{TFIDF}}^{(j)} \in \mathbb{R}^{(16 \times n_g) \times 1}$ be the concatenated TF-IDF scores belonging to the j -th patient. To extract features, we use PCA to reduce the dimension of $(A_{\text{TFIDF}}^{(1)}, \dots, A_{\text{TFIDF}}^{(N)})^\top \in \mathbb{R}^{N \times (16 \times n_g)}$ to $N \times 512$, i.e., for patient j , we obtain a feature vector $X_j \in \mathbb{R}^{512}$. Then, we use a fully connected neural network with one hidden layer with 32 nodes, and the results are presented in Supplementary Figure S8.



Neural Network						
Paradigm	Error1	Error23	Error21	Error31	Error32	Overall
classical	0.324	0.113	0.220	0.073	0.215	0.322
H-NP	0.134	0.030	0.459	0.301	0.271	0.402

Figure S8: The distributions and averages of approximate errors for the neural network approach and the H-NP classifier. “error1”, “error23”, “error21”, “error32”, “overall” correspond to $R_{1\star}(\hat{\phi})$, $R_{2\star}(\hat{\phi})$, $P_2(\hat{Y} = 1)$, $P_3(\hat{Y} = 1)$, $P_3(\hat{Y} = 2)$ and $P(\hat{Y} \neq Y)$, respectively.